Mechanical Systems and Signal Processing 99 (2018) 83–106

Contents lists available at ScienceDirect

Mechanical Systems and Signal Processing

journal homepage: www.elsevier.com/locate/ymssp

Step responses of a torsional system with multiple clearances: Study of vibro-impact phenomenon using experimental and computational methods

Pradeep Sharma Oruganti, Michael D. Krak, Rajendra Singh *

Acoustics and Dynamics Laboratory, NSF Smart Vehicle Concepts Center, Department of Mechanical and Aerospace Engineering, The Ohio State University, Columbus, OH 43210, USA

ARTICLE INFO

Article history:
Received 31 December 2016
Received in revised form 24 May 2017
Accepted 31 May 2017

Keywords:
Transient responses
Non-linear models
Experimental dynamics
Vibro-impact phenomena
Metrics for impulsive events

ABSTRACT

Recently Krak and Singh (2017) proposed a scientific experiment that examined vibro-impacts in a torsional system under a step down excitation and provided preliminary measurements and limited non-linear model studies. A major goal of this article is to extend the prior work with a focus on the examination of vibro-impact phenomena observed under step responses in a torsional system with one, two or three controlled clearances. First, new measurements are made at several locations with a higher sampling frequency. Measured angular accelerations are examined in both time and time-frequency domains. Minimal order non-linear models of the experiment are successfully constructed, using piecewise linear stiffness and Coulomb friction elements; eight cases of the generic system are examined though only three are experimentally studied. Measured and predicted responses for single and dual clearance configurations exhibit double sided impacts and time varying periods suggest softening trends under the step down torque. Non-linear models are experimentally validated by comparing results with new measurements and with those previously reported. Several metrics are utilized to quantify and compare the measured and predicted responses (including peak to peak accelerations). Eigensolutions and step responses of the corresponding linearized models are utilized to better understand the nature of the non-linear dynamic system. Finally, the effect of step amplitude on the non-linear responses is examined for several configurations, and hardening trends are observed in the torsional system with three clearances.

1. Introduction

In a recent article, Krak and Singh [1] developed a controlled, non-rotating type tabletop laboratory experiment to acquire benchmark step response measurements for a torsional system with one or two clearances. Preliminary measurements and non-linear models were presented (under step down torque input) to verify the scientific utility of experiment. The goal of this article is to extend the prior work [1] by making additional measurements with a higher sampling frequency, and to validate non-linear models and quantify the vibro-impact behavior. The torsional system is computationally generalized to include up to three clearances so that various non-linear configurations may be examined under alternate step excitations profiles.

* Corresponding author.
E-mail address: singh.3@osu.edu (R. Singh).

http://dx.doi.org/10.1016/j.ymssp.2017.05.043
0888-3270/

Discontinuous non-linear elements (including backlashes and multi-valued spring) introduce vibro-impacts in many practical systems [2–13]. Prime examples of typical noise and vibration problems in automotive systems include gear rattle and driveline clunk [2,5,14–25]. In particular, the neutral or drive gear rattle is observed in automotive drivetrains with several gear pairs with backlash elements when excited by a pulsating torque with minimal mean (constant) torque [2,5,14–16]. In contrast, the clunk problem is associated with a rapid change in or reversal of the mean torque due to sharp throttle demand in vehicles (for instance under abrupt tip-in or tip-out conditions); it leads to high amplitude non-linear torsional motions and impulsive loads in the system [17–25]. Several researchers have attempted to experimentally [8,9,17,20,23,26] and/or computationally [20–27] address these problems. Three types of commercial non-linear codes have essentially been used: finite element method, multi-body dynamics or 1-D multi-physics type calculations [20–27]. Other investigators have employed minimal order lumped parameter models where key non-linear or piecewise linear stiffness and friction/damping elements are described [17–20,27]. Although prior studies with real world components provide system level insights to solve particular noise and vibration problems, they do not yield a fundamental understanding of the underlying physics associated with multiple clearances. In addition, while there are many investigations on the steady state responses of strongly discontinuous systems [6,7,28–32], the literature on the transient responses of such mechanical system is sparse [16,17,27]. This motivated Krak and Singh [1] to develop a new experiment that isolated the pure clearance elements in a controlled manner; this article is a continuation of that effort.

To overcome the stated deficiencies of the literature, the following major objectives are formulated: (1) Conduct new measurements on the experiment described by Krak and Singh [1] with a higher sampling frequency at several sensor locations, and examine time or time-frequency domain characteristics (such as their time-varying periods) of single and dual clearance systems under step down torque excitation; (2) Develop and validate minimal order non-linear models and provide some explanations using eigensolutions and step responses of the corresponding linearized system; and (3) Investigate several impulsive response metrics (as reported in the literature for the clunk problem [18,19]) and examine the role of step excitation profile and amplitude on the nature of vibro-impact phenomena.

2. Problem formulation and non-linear model

The problem posed by Krak and Singh [1] is generalized, in the context of a minimal order non-linear system, to accomplish the stated objectives. Consider a three degree of freedom (3DOF) positive-definite torsional system with three possible clearance non-linearities as displayed in Fig. 1a. The torsional inertia is given by J, with subscripts A, B and C denoting their locations. The angular displacement, velocity and the angular acceleration variables are given by $\{\theta(t), \dot{\theta}(t), \ddot{\theta}(t)\}$ where t is

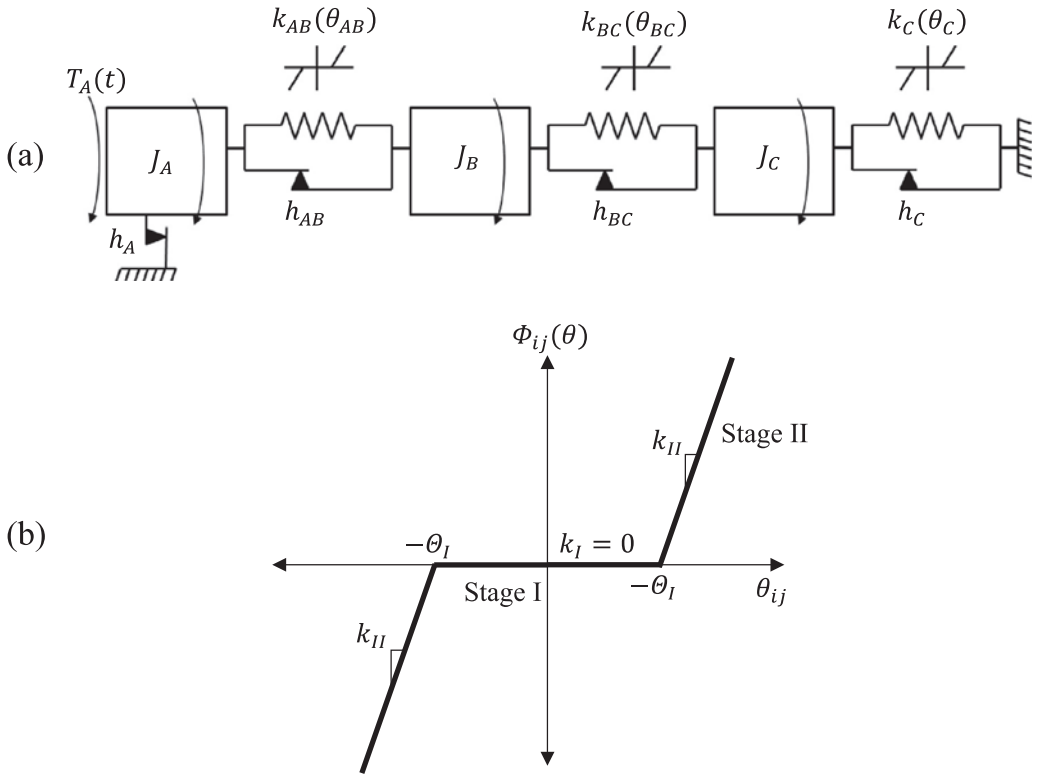

Fig. 1. Example case: 3DOF torsional system with three possible clearance and four Coulomb friction elements. (a) Schematic of the torsional system; and (b) elastic torque, $\Phi(\theta)$, relationship at the clearance non-linearity. Refer to Table 1 for the eight cases that are studied in this article.

the time. While the subscripts A, B and C are used to describe the absolute motions, subscripts AB and BC signify the relative motions such as $\theta_{AB} = \theta_A - \theta_B$ and $\theta_{BC} = \theta_B - \theta_C$. Four Coulomb friction elements are included in Fig. 1a as well. The non-linear governing equations for the system are expressed below, where Φ and Ψ are the elastic and dissipative torque terms respectively:

$$\begin{aligned} &J_A\ddot{\theta}_A + \Psi_A(\dot{\theta}_A) + \Psi_{AB}(\dot{\theta}_{AB}) + \Phi_{AB}(\theta_{AB}) = T_A(t), \\ &J_B\ddot{\theta}_B - \Psi_{AB}(\dot{\theta}_{AB}) + \Psi_{BC}(\dot{\theta}_{BC}) - \Phi_{AB}(\theta_{AB}) + \Phi_{BC}\theta_{BC} = 0, \\ &J_C\ddot{\theta}_C - \Psi_{BC}(\dot{\theta}_{BC}) + \Psi_C(\dot{\theta}_C) - \Phi_{BC}\theta_{BC} + \Phi_C(\theta_C) = 0. \end{aligned} \tag{1a-c}$$

The external transient torque $T_A(t)$ is applied only at location A. The elastic torque term for the clearance non-linearity between the i^{th} and j^{th} inertial elements is described by a piecewise linear stiffness $k_{ij}(\theta_{ij})$ with two stages (I and II) as shown in Fig. 1b:

$$k_{ij}(\theta_{ij}) = k_I + (k_{II} - k_I)\Xi(|\theta_{ij}| - \Theta_I). \tag{2}$$

In the above equation, Ξ is the unit step (Heaviside) function and stage I is the clearance or gap with the stage transition occurring at an angular displacement of $\pm\Theta_I$. Stage II is assumed to be given by a linear spring element as the Hertzian type contact is ignored in this paper. The elastic torque, $\Phi_{ij}(\theta_{ij})$ as displayed in Fig. 1b, is defined as:

$$\Phi_{ij}(\theta_{ij}) = k_I\theta_{ij} + \mathrm{sgn}(\theta_{ij})(k_{II} - k_I)(|\theta_{ij}| - \Theta_I)\mathrm{sgn}(|\theta_{ij}| - \Theta_I). \tag{3}$$

Here, $\mathrm{sgn}(\dot{\theta}) = \dot{\theta}/|\dot{\theta}|$ is the well-known signum function, employed to take the relative direction of motion into consideration. Each dissipative element (h) is modeled by the following hysteretic Coulomb friction as:

$$\Psi_{ij}(\dot{\theta}_{ij}) = h_{ij}\tanh(\sigma\dot{\theta}_{ij}). \tag{4}$$

In the above equation, a hyperbolic tangent approximation (with σ as the regularizing factor) is utilized to smoothen the transition and reduce the computational effort [33]. The ideal step excitation (down or up) is mostly considered in both experimental and computational studies. It is defined below using the initial, T_0 and final, T_f torques as:

$$T_A(t) = T_0[1 - \Xi(t)] + T_f\Xi(t), \quad t \geqslant 0. \tag{5}$$

Since it would be difficult to apply an abrupt excitation in physical systems, a step-like excitation is also considered. The exponentially decaying excitation is described below where the parameter β is used to adjust the decay rate:

$$T_A(t) = [1 - \Xi(t)] + e^{-t/\beta}\Xi(t). \tag{6}$$

Eight subsets of the torsional system of Fig. 1a, as listed in Table 1, are considered. Case I is a linearized system where all three elastic elements are in stage II; this case is also denoted as a no clearance system. Here, the dry friction damping elements may be linearized or replaced with equivalent viscous damping coefficients. Case II includes only one clearance non-linearity at AB and a linear compliant spring at BC. In contrast, the single clearance non-linearity is now included at C for Case III. Further, two clearances are included in Cases IV, V and VI; these clearances are at BC and C in Case IV, at AB and C in Case V and at AB and BC in Case VI; the linear spring element is at location AB in Case IV, BC in Case V and C in Case VI. Note that Case VII is an effective single degree of freedom (SDOF) configuration with a single clearance non-linearity between an effective inertial element and the ground. Finally, Case VIII includes three clearances concurrently as shown in Fig. 1a. All configurations (except Case I) consider non-linear dry friction elements as defined by Eq. (4).

To define an underlying time period, Case I is simplified as an effective SDOF linear system by grounding J_C and rigidly connecting J_C and J_B. The effective (with subscript 'e') torsional inertia is $J_e = J_A + J_B$ and the spring element at location BC is linear. The governing equation is given by:

$$J_e\ddot{\theta}_e + C\dot{\theta}_e + k_{BC}\theta_e = T_A(t). \tag{7}$$

Here the dry friction damping is replaced with an equivalent viscous damping coefficient C. The natural period $\tau_n(= 2\pi/\omega_n)$ of this SDOF system is as follows, where ω_n is the natural frequency (rad/s):

Table 1
Eight cases of the 3DOF non-linear system (Fig. 1) examined using computational and experimental methods.

Case	Number of clearances and location(s)	Effective order of system	Experimental evaluation (Fig. 2)
I	0	3DOF	No
II	1 (AB)	2DOF	Yes
III	1 (C)	2DOF	Yes
IV	2 (BC and C)	3DOF	No
V	2 (AB and C)	3DOF	Yes
VI	2 (AB and BC)	3DOF	No
VII	1 (AB)	SDOF	No
VIII	3 (AB, BC and C)	3DOF	No

$$\tau_n = 2\pi\sqrt{\frac{J_e}{k_{BC}}}. \tag{8}$$

This τ_n is used to normalize the time and motion variables which are described by a bar above the symbol. The normalized time ($\bar{t}$), acceleration ($\ddot{\bar{\theta}}(\bar{t})$), velocity ($\dot{\bar{\theta}}(\bar{t})$) and displacement ($\bar{\theta}(\bar{t})$) are described as:

$$\bar{t} = \frac{t}{\tau_n}, \quad \bar{\theta}_i(\bar{t}) = \frac{\theta_i(\bar{t})}{\Theta_I}, \quad \dot{\bar{\theta}}_i(\bar{t}) = \frac{\dot{\theta}_i(\bar{t})\tau_n}{\Theta_I}, \quad \ddot{\bar{\theta}}_i(\bar{t}) = \frac{\ddot{\theta}_i(\bar{t})\tau_n^2}{\Theta_I}. \tag{9a-d}$$

The external torque expression is also normalized using the initial torque value (T_0 at $t = 0$) or a comparable step height as:

$$\bar{T}(\bar{t}) = \frac{T_A(\bar{t})}{T_0}, \quad \bar{t} \geqslant 0. \tag{10}$$

3. Experimental studies

The experiment proposed by Krak and Singh [1] is designed to implement only a few subsets of Fig. 1a and Table 1. These include the system with one and two clearances corresponding to Cases II (or III) and IV respectively. Since only the preliminary measurements were reported in [1], the system has been reassembled and additional measurements are acquired and analyzed as part of this article. Unlike the previous study [1] that limited the sampling frequency to 12.8 kHz, a much higher sampling frequency (51.2 kHz) is selected to ensure that the impulsive responses are adequately captured [34].

The experiment of Fig. 2a consists of a torsion arm that is rigidly connected to the disks and shaft. An electromagnetic mass drop arrangement is attached to the torsion arm and is used to provide the step down $T_A(t)$ excitation [1]. The electromagnetic mass drop (m) coupled with the length of the torsion arm (l) produces the initial torque $T_0 = 0.5mgl$ where g

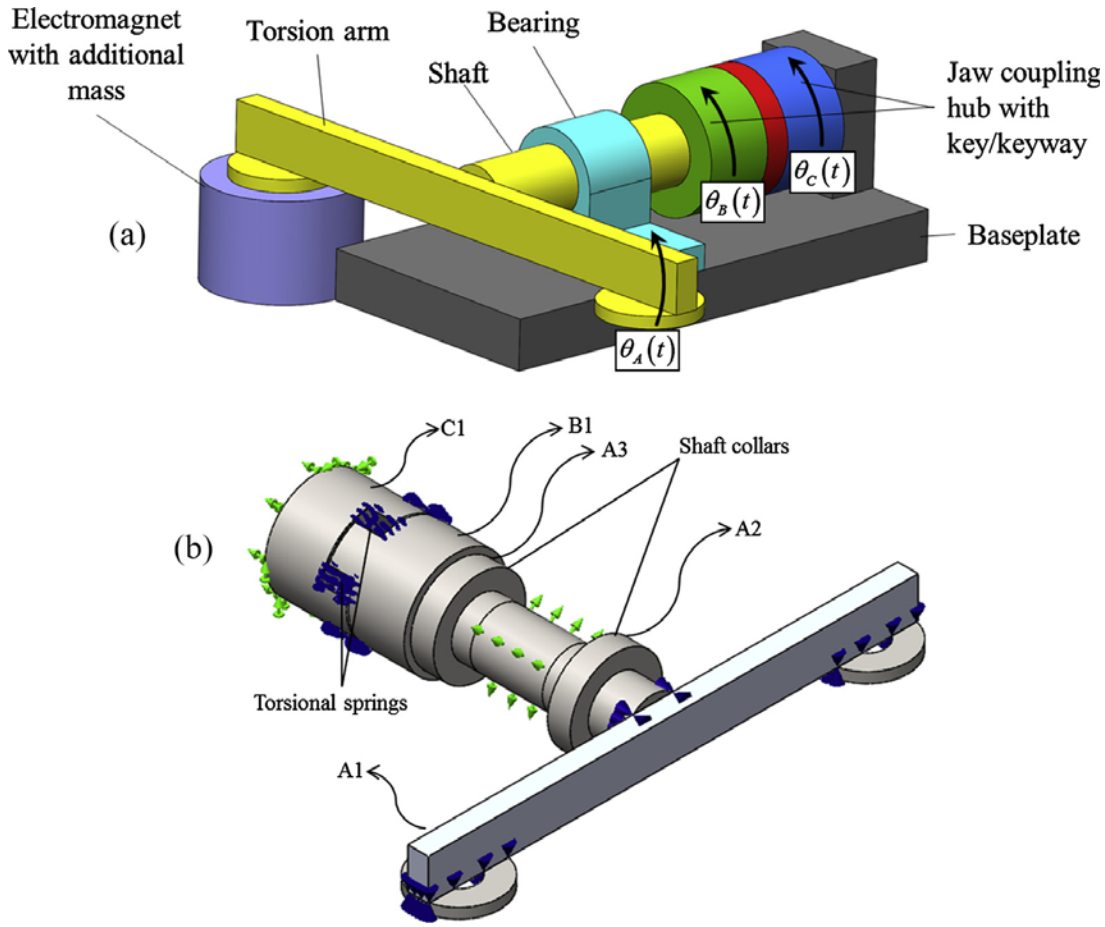

Fig. 2. Experiment used to implement the non-linear torsional system of Fig. 1a and to study step down responses. (a) Solid model displaying various components; and (b) finite element model of the experiment and locations of the translational accelerometers used for measurements (A1, A2, A3, B1 and C1).

is the acceleration due to gravity. A set of disks are symmetrically attached at the ends of the torsion arm (for ease in placement of the mass drop) so that the final torque value, T_f, is close to zero. Two identical jaw coupling hubs are coupled through a set of six torsional springs. The experimental system is lumped (like Fig. 1a) into three inertial bodies (J_A, J_B and J_C) where J_B and J_C are the coupling hubs with J_C being closer to ground. The element J_A includes the inertias of the shaft coupled with the torsion arm, disks and shaft collars. The second coupling hub is fixed to the base using a steel plate. Keys and keyways on the shaft become the sources of two clearances ($k_{AB}(\theta_{AB})$ and $k_C(\theta_C)$) as they interface with the coupling hubs. The shaft collars are used to assemble the system and also to improve the alignment of the shaft bearing and the coupling hubs. This process tends to reduce the dry friction as well within the torsional system. Further, a Teflon sheet is used between the sliding surfaces to minimize the friction.

A finite element model of the experiment is shown in Fig. 2b. The shaft is balanced on a sleeve bearing, and is constrained in the radial direction as indicated by the arrows in Fig. 2b. The vibration modes of the experimental set up are computed by a finite element code [35]. The analysis indicates the presence of 4 flexural modes of the torsion arm between 310 Hz and 620 Hz, two torsional modes of the arm at 1690 Hz and 1720 Hz followed by a flexural mode of the shaft at 2000 Hz. Coupled shaft and arm flexural modes are found beyond 2000 Hz.

The set screws are loosened or tightened so as to implement three specific Cases (II, III and IV) of Table 1. The vibro-impact phenomena are measured for the three configurations (two with a single clearance and one with dual clearances) using five translational accelerometers [36]. As illustrated in Fig. 2b, locations are as follows: A1 on the torsion arm, A2 and A3 on the shaft collars and B1 and C1 on the two coupling hubs. Other cases of Table 1 are only computationally examined.

First, consider Case II that includes only one clearance non-linearity at AB and a linear compliant spring at BC. It is experimentally implemented first by loosening the set screw on J_B creating a clearance between inertial elements A and B ($\Phi_{AB}(\bar{\theta}_{AB})$). The set screw on J_C is tightened thus effectively grounding C. The torsional springs between the coupling hubs B and C ($k_{BC}\bar{\theta}_B$) are assumed to be linear. The resulting system could be described by an effective two degree of freedom (2DOF) system where J_A and J_B are rigidly connected to form the J_A+J_B element. The governing equations of motion, in the normalized form, are obtained from Eqs. (1), (8) and (9) as follows:

$$\begin{aligned} &J_A\ddot{\bar{\theta}}_A + \Psi_A(\dot{\bar{\theta}}_A) + \Psi_{AB}(\dot{\bar{\theta}}_{AB}) + \Phi_{AB}(\bar{\theta}_{AB}) = \bar{T}(\bar{t}),\\ &J_B\ddot{\bar{\theta}}_B - \Psi_{AB}(\dot{\bar{\theta}}_{AB}) + \Psi_{BC}(\dot{\bar{\theta}}_{BC}) - \Phi_{AB}(\bar{\theta}_{AB}) + k_{BC}\bar{\theta}_B = 0. \end{aligned} \tag{11a-b}$$

Next, Case III of Table 1 (again with a single clearance) is achieved by tightening the set screws on J_B, creating a rigid link between A and B, and then loosening the set screw on J_C, creating a clearance between C and the ground ($\Phi_C(\bar{\theta}_C)$). The step down torque excitation is now applied to the combined inertia of A and B. The equations of motion (in the normalized form) for this 2DOF system are:

$$\begin{aligned} &J_e\ddot{\bar{\theta}}_e + \Psi_A(\dot{\bar{\theta}}_e) + \Psi_{BC}(\dot{\bar{\theta}}_e) + k_{BC}\bar{\theta}_e = \bar{T}(\bar{t}),\\ &J_C\ddot{\bar{\theta}}_C - \Psi_{BC}(\dot{\bar{\theta}}_{BC}) + \Psi_C(\dot{\bar{\theta}}_C) - k_{BC}\bar{\theta}_{BC} + \Phi_C(\bar{\theta}_C) = 0. \end{aligned} \tag{12a-b}$$

Finally, Case V of Table 1 (with two clearances) is implemented by loosening both sets of screws on J_B and J_C thereby creating clearances at locations AB and C respectively. The non-linear governing equations for the 3DOF system are defined as:

$$\begin{aligned} &J_A\ddot{\bar{\theta}}_A + \Psi_A(\dot{\bar{\theta}}_A) + \Psi_{AB}(\dot{\bar{\theta}}_{AB}) + \Phi_{AB}(\bar{\theta}_{AB}) = \bar{T}(\bar{t}),\\ &J_B\ddot{\bar{\theta}}_B - \Psi_{AB}(\dot{\bar{\theta}}_{AB}) + \Psi_{BC}(\dot{\bar{\theta}}_{BC}) - \Phi_{AB}(\bar{\theta}_{AB}) + k_{BC}\bar{\theta}_{BC} = 0,\\ &J_C\ddot{\bar{\theta}}_C - \Psi_{BC}(\dot{\bar{\theta}}_{BC}) + \Psi_C(\dot{\bar{\theta}}_C) - k_{BC}\bar{\theta}_{BC} + \Phi_C(\bar{\theta}_C) = 0. \end{aligned} \tag{13a-c}$$

The signal from each translational accelerometer is converted into angular acceleration by dividing the measured acceleration by its radial distance [1]. In addition to examining the measurements in the time domain, the Short Term Fourier Transforms (STFT) of the accelerations, $S\{\ddot{\theta}(n,\Delta t)\}$ are estimated where Δt is the time resolution and n is the sequence index. The resulting spectrograms [37] are calculated with the Hamming window where the key sampling parameters include a frequency resolution (Δf) of 25 Hz and a time resolution (Δt) of 80.1 μs. The STFT results are further verified by the Fast Fourier Transform $\mathscr{F}(\ddot{\theta}_{w,j})$ with a frequency resolution of 0.8 Hz and a signal length of 65,536 discrete points of the time history say at the j^{th} location; here, the subscript 'w' denotes that the Hanning window is used to weight the acceleration signal. Note that no window is utilized for acquiring time domain results unless needed for a metric calculation.

Analysis of the accelerations, at the torsion arm (A1) indicates that it picks up signals mostly below 50 Hz which correspond to the rigid body modes of the experimental system (including its base) and hence signals from location A1 are not used any further. The measured accelerations on the shaft and shaft collars (using sensors A2 and A3 respectively) yield a wideband spectrogram peaking around 2000 Hz indicating that higher natural modes are being excited. The lumped torsional model of Fig. 1a (as defined in Section 2) obviously does not predict any such elastic deformation modes. Therefore, measurements from A2 and A3 locations are not considered for the validation of the non-linear model. Further, measured spectrograms from the coupling hubs (B1 and C1) indicate that modes between 700 and 900 Hz are being excited. From

the eigenvalue problem of the linearized system (Case V, as discussed later in Section 6), two torsional modes of the system are calculated to be 742 Hz and 770 Hz.

Typical time and frequency contents of the measured accelerations are shown in Fig. 3 for the dual clearance configuration (Case V) at 5 locations. An additional accelerometer (B2) is placed orthogonal to B1 (rotated by 90°) to check for a variability in the measurements due to a preference of the circumferential location(s). A close match between accelerations B1 and B2 on the coupling hubs is found and this confirms that B1 measurements are suitable for the torsional system analysis. Only measurements from B1 (or simply B) and C locations would be utilized further to validate the non-linear models (in Section 4) and to quantify the impulsive metrics (in Section 5).

4. Experimental validation of non-linear models

The non-linear models, as given by Eqs. (11)–(13) for Cases II, III and V are first numerically solved [37] under a step down torque input $\bar{T}$ = 1.0 to 0. The resolution of the resulting time array and the maximum allowable integration time-step are chosen to correspond with the sampling period (19.5 μs) used in the new measurements. The resulting motion predictions are compared with measurements in the normalized manner as defined by Eqs. (9) and (10).

First, the dual clearance configuration (Case V) is examined in Fig. 4 to illustrate the angular displacement time histories from the model; predictions of $\bar{\theta}_{AB}(\bar{t})$ in Fig. 4a and $\bar{\theta}_{C}(\bar{t})$ in Fig. 4c clearly show double sided impacts. Whenever $\bar{\theta}_{AB}(\bar{t})$ or $\bar{\theta}_{C}(\bar{t})$ crosses the stage transitions at $\pm\Theta_I$, a double sided impact is generated. Similar observations are also made for the single

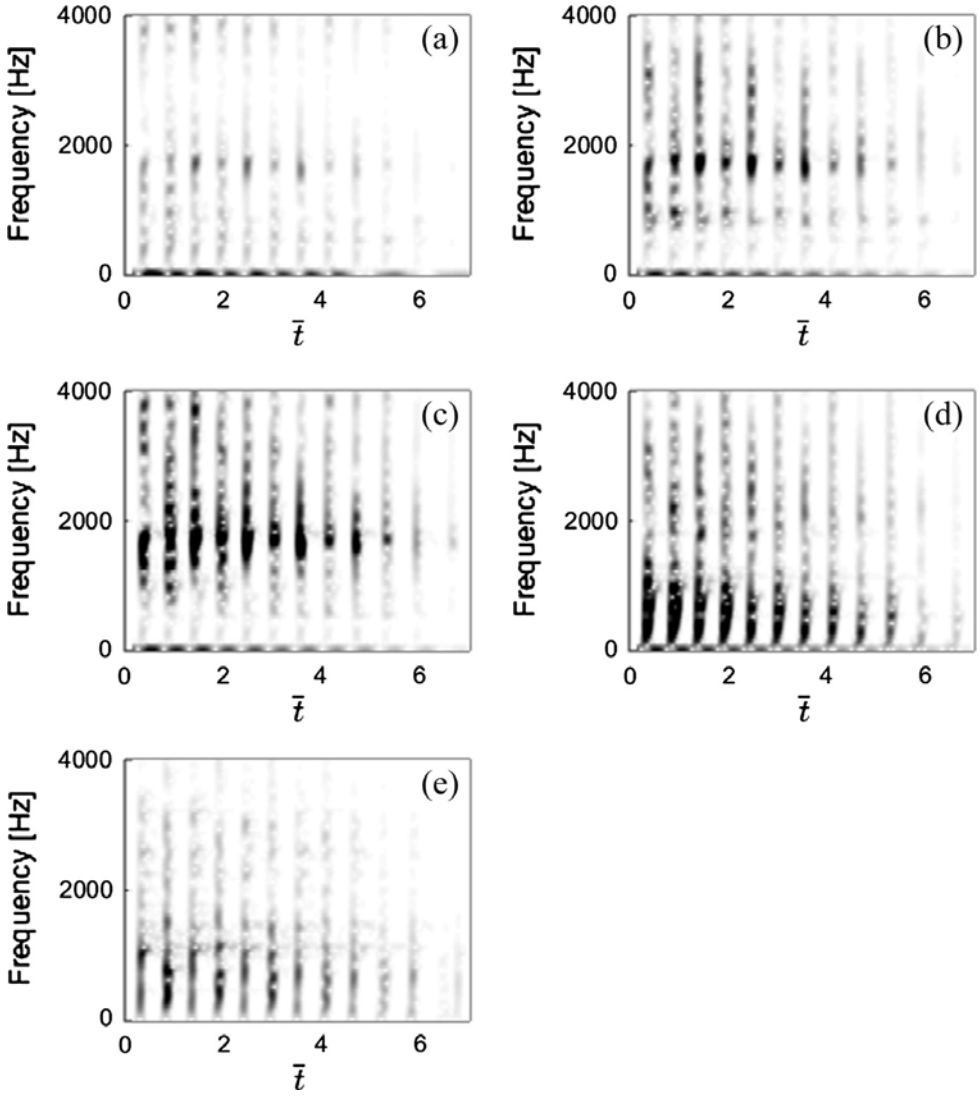

Fig. 3. Spectrograms of measured angular accelerations with the experiment in the dual clearance configuration under step down excitation ($\bar{T}$ = 1.0 to 0). (a) On the torsion arm (A1); (b) on the first shaft collar (A2); (c) on the second shaft collar (A3); (d) on the first coupling hub (B1); and (e) on the second coupling hub (C). Refer to Fig. 2 for sensor locations and components.

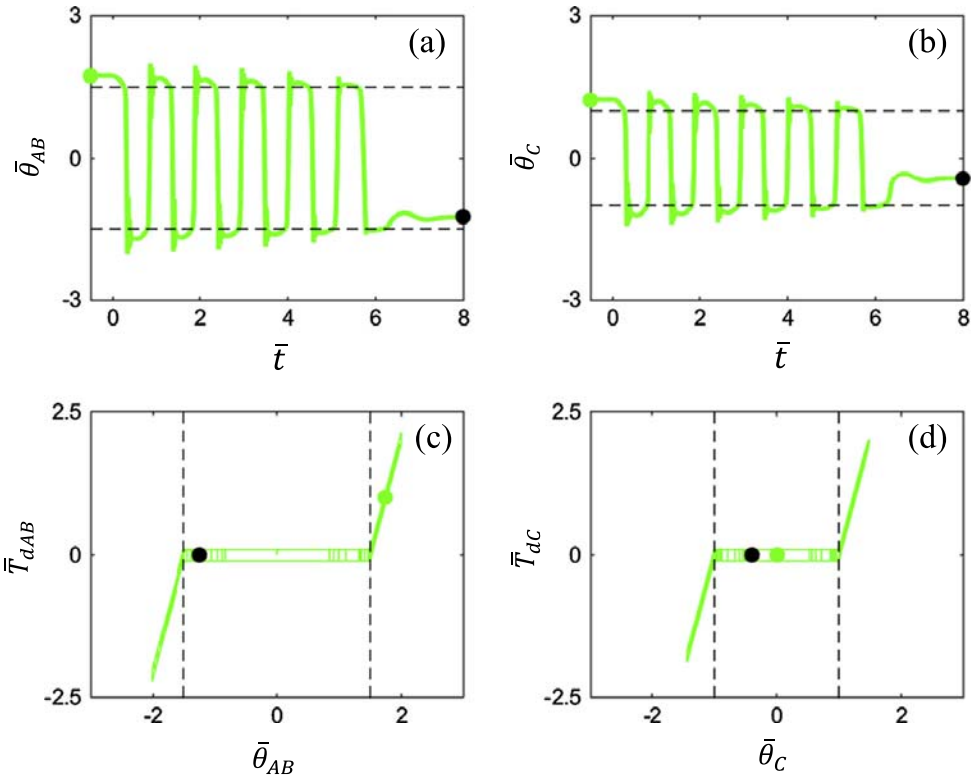

Fig. 4. Predicted time histories of relative angular displacements and dynamic torques for the dual clearance configuration (Case IV) under step down torque ($\bar{T}$ = 1.0 to 0). (a) $\bar{\theta}_{AB}(\bar{t})$; (b) $\bar{T}_{dAB}(\bar{t})$ vs. $\bar{\theta}_{AB}(\bar{t})$; (c) $\bar{\theta}_C(\bar{t})$; and (d) $\bar{T}_{dC}(\bar{t})$ vs. $\bar{\theta}_C(\bar{t})$. Key: (●) – $\bar{\theta}(0)$; (●) – $\bar{\theta}(10)$; (—) – clearance transition; and (—) – non-linear model.

clearance configurations (Cases II and III) though their results are not displayed in Fig. 4 for the sake of brevity. Typical dynamic torque, T_d, through the clearance non-linearity between the *ith* and *jth* inertial elements is defined using Eqs. (2) and (3) as:

$$T_{d,ij}(t) = \Phi_{ij}(\theta_{ij}) + \Psi_{ij}(\dot{\theta}_{ij}). \tag{14}$$

The T_d value is also normalized by T_0 and is displayed in Fig. 4b and d. Observe that the initial and final dynamic torque values reside in stage II and stage I respectively of the static $k_{ij}(\theta_{ij})$ curve under the step down torque. The phase plane plots for the relative displacements $(\bar{\theta}_{AB})$ against corresponding relative velocity $(\dot{\bar{\theta}}_{AB})$ are shown in Fig. 5a over $\bar{t}$ = 0 to 1.0 for one single clearance configuration (Case II) and one dual clearance configuration (Case V). Observe the existence of two equilibrium points beyond the clearance transitions indicating that the system is well behaved as it does not stay much in the gap regime; no chaos is observed. Comparisons of dynamic torque $(\bar{T}_{dAB})$ through clearance AB against relative angular displacement $(\bar{\theta}_{AB})$ is shown in Fig. 5b and against $\bar{t}$ in Fig. 5d between Cases II and V. The peak-peak acceleration amplitudes are slightly higher in the single clearance configuration (Case II) than in the dual clearance case (Case V). Observe the linear decay of impulsive amplitudes in Fig. 5c indicating the presence of dry friction in the system.

Predicted accelerations are compared with measurements in Fig. 6 for Case V and in Fig. 7 for Cases II and III. Note that a Θ_I value of 0.1° is used at location C but a value of 0.15° is used at location AB, making the system slightly asymmetrical. Note that reassembly of the experiment might have slightly changed the clearance values, which is common in practical systems with discontinuous non-linearities; the 0.1° clearances were assumed to be symmetric in the preliminary work reported by Krak and Singh [1]. Comparisons suggest a good match between the measured and predicted $\ddot{\bar{\theta}}$ over $\bar{t}$ = 0 to 10. The discrepancy between measured and predicted peak-peak amplitudes can be explained by the fact that an impact damping formulation is not included in the non-linear model [13]. Another possible reason for such a mismatch might be due to the computational issues given a strongly non-linear system since the ratio of k_{II} to k_I is unbounded. Further, measured and predicted peak-peak amplitudes are compared with preliminary studies reported by Krak and Singh [1] for the following configurations: Case II at locations B and Case V at locations B and C. A large difference in the peak-peak amplitudes might arise from the fact that the accelerations values were previously normalized [1] by $\theta_{BC\_max}\tau_n^2$, where $\theta_{BC\_max} = T_0/k_{BC}$, whereas they are normalized (in this article) by using Θ_I (Eq. (9d)). The peak-peak acceleration amplitude of the impact is quantified in terms of metric Q_3 (see Section 5 for other metrics). For the j^{th} inertial element, at any particular impact (say k), Q_3 is defined as $\ddot{\bar{\theta}}^{pp}_{j,k} = \max(\ddot{\bar{\theta}}_{j,k}) - \min(\ddot{\bar{\theta}}_{j,k})$. Since a large dynamic range is observed in the Q_3 values, the log-

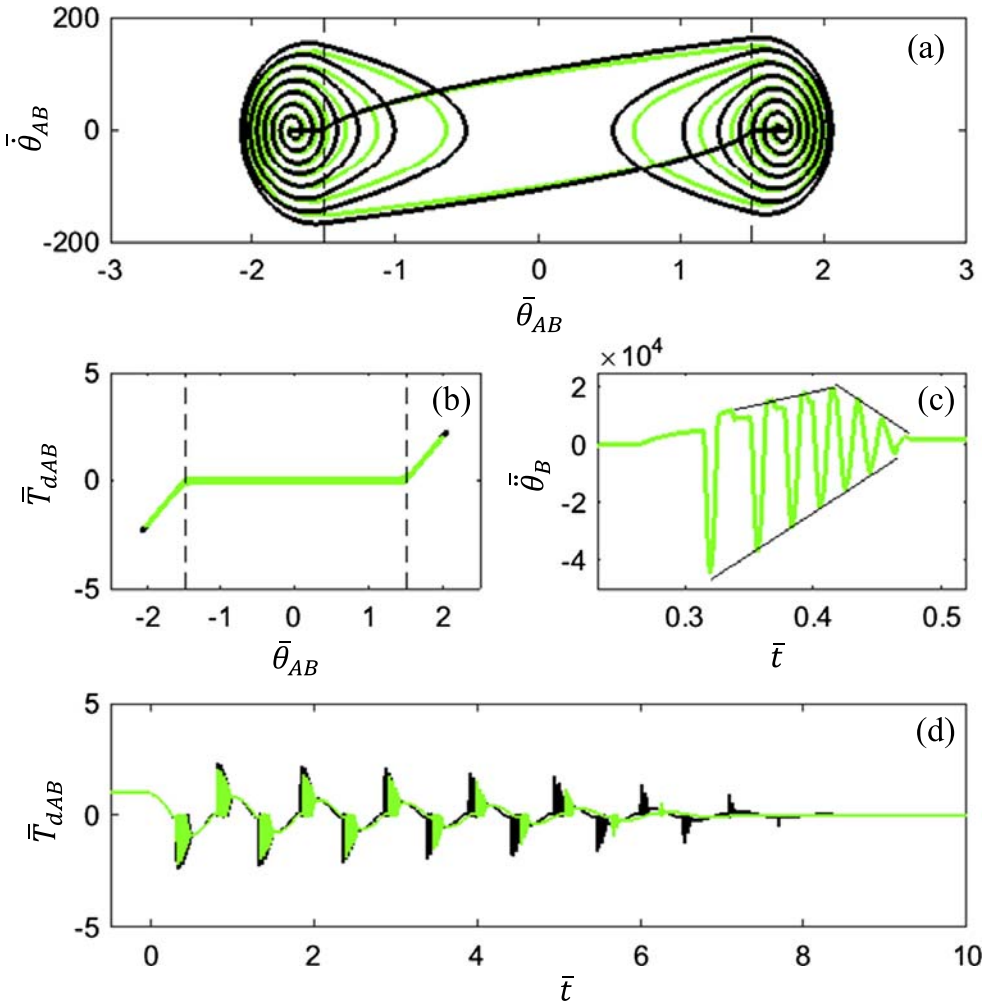

Fig. 5. Comparison of responses between single clearance (Case II) and dual clearance (Case V) configurations given a step down torque ($\bar{T}$ = 1.0 to 0). (a) $\dot{\bar{\theta}}_{AB}(\bar{t})$ vs. $\bar{\theta}_{AB}(\bar{t})$ from $\bar{t}$ = 0 to 1.0; (b) $\bar{T}_{dAB}$ vs. $\bar{\theta}_C(\bar{t})$; (c) first impact as predicted in $\ddot{\bar{\theta}}_B$; and (d) $\bar{T}_{dAB}$ vs. $\bar{T}$. Key: (▬) – Case II; (▬) – Case V; (—) – clearance transition; and (–) – curve fits of the linear decay of peak amplitudes. Refer to Table 1 for the identification of the cases.

arithmic value is defined by $20\log_{10}Q_3$, dB re 1.0 rad/s^2. Table 2 compares all measurements and predictions when they are normalized according to (Eq. (9)) and the prior acceleration values of [1] are rescaled. Only Q_3 values (rounded off to the nearest dB) are summarized in Table 2. In general, new measured peak-peak acceleration values are slightly higher than those reported by Krak and Singh [1] due to the higher sampling frequency used. For example, the absolute peak-peak acceleration of the first impact at location B for Case V as reported by Krak and Singh [1] is 26,713 rad/s^2 with a sampling frequency of 12.8 kHz whereas it is measured to be 40,810 rad/s^2 using a sampling frequency of 51.2 kHz.

The non-linear responses are characterized by measuring the time-varying period, $\bar{\tau}_{osc}(\bar{t}_{osc})$ of impacts which is the normalized time between impact number k and k + 2. The subscript '*osc*' is used to indicate time varying nature as the terminology used previously [1] is retained for the sake of consistency. The general form for a curve fit of measurements is given by the following where the time variable is $\bar{t}_{osc} = 0.5(\bar{t}_{k+2} + \bar{t}_k)$ and a_0, a_1 and a_2 are the coefficients:

$$\bar{\tau}_{osc} = a_0 + a_1\bar{t}_{osc} + a_2\bar{t}^2_{osc}. \tag{15}$$

For Case V, the coefficients at locations B (Fig. 8d) and C (Fig. 8c) are: a_0 = 1.045, a_1 = −0.013 and −0.01, and a_2 = 0.0059 and 0.0052 respectively. The curve fit results for Case II at location B (Fig. 8b) a $\bar{\tau}_{osc}(\bar{t}_{osc})$ re: a_0 = 1.043, a_1 = −0.0263 and a_2 = 0.0071. For Case III (Fig. 8a), the coefficients at location C are: a_0 = 0.982, a_1 = −0.0035 and a_2 = −0.0006. The curve fits are compared in Fig. 8 with predicted time periods (at locations B and C) for each configuration. Trends from these comparisons for the step down torque indicate a net softening effect. Finally, a sensitivity analysis is conducted to investigate the variations in predictions with changes in (a) k; (b) h; and (c) Θ_I. Comparison between the measured and predicted periods are shown in Fig. 9. Observe that as Θ_I increases, the predicted by the non-linear model match closely with measurements. However, the predicted $\bar{\tau}_{osc}(\bar{t}_{osc})$ are relatively insensitive to a variation in k or h indicating the critical role played by the clearance in governing the non-linear dynamic responses. This observation is further reinforced by the results of a sensitivity analysis where it is observed that the peak-peak values of the impacts reduce only by 0.2% in the nonlinear models when the

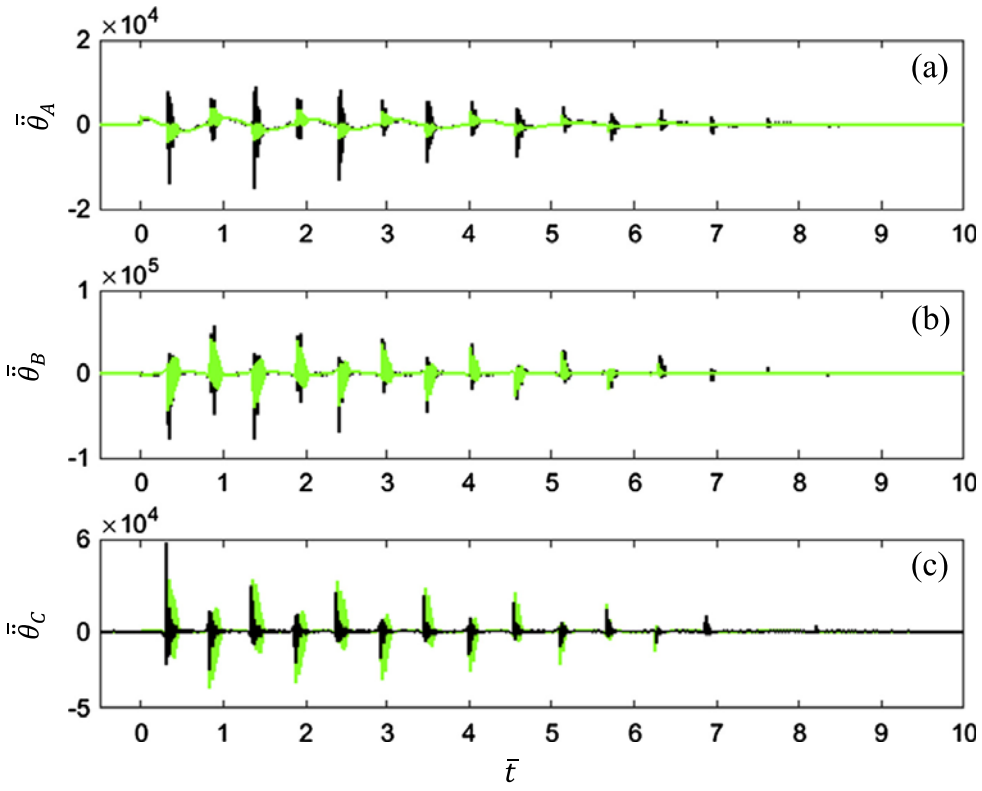

Fig. 6. Experimental validation of the non-linear model for the dual clearance configuration (Case V) by comparing $\bar{\theta}(\bar{t})$ under a step down torque ($\bar{T}$ = 1.0 to 0). (a) $\bar{\theta}_A(\bar{t})$; (b) $\bar{\theta}_B(\bar{t})$; and (c) $\bar{\theta}_C(\bar{t})$. Key: (▬) – measured; and (▬) – predicted.

regularizing factor (σ) is increased from 50 to 99 (smoother to sharper). Similar behavior is observed for the single clearance configurations (Cases II and III).

5. Quantification of impulsive responses

Several metrics, as suggested by Crowther et al. [18] and Oh et al. [19], are used to quantify the measured and predicted impulsive accelerations; the terminology used previously [18,19] is retained for the sake of consistency and comparative assessment. First, consider the total number of impacts, Q_1, observed over the entire time history of the response. An impact occurs whenever the relative displacement crosses Θ_l; it is observed as a 'spike' in the acceleration signal. Next, the type of impact (described by metric Q_2) is determined from the validated non-linear model by tracking the relative angular displacement(s) at the clearance(s). If $\bar{\theta}_{ij}$ does not cross Θ_l, no impact occurs; a single sided impact (si) is described by a response where $\bar{\theta}_{ij}$ crosses Θ_l only on one side of the origin; and a double sided impact (di) is the one where the stage transition is crossed on both sides. As mentioned before, only double sided impacts (under the step down torque from $\bar{T}$ = 1.0 to 0) occur in the three experimental configurations (Cases II, III and V).

As mentioned in Section 4, Q_3 is used to quantify the impulsive peak-peak acceleration. Further, during an impact, the inertial element (say j) attains its maximum angular velocity immediately after the impact (say k). It is described by a velocity metric, $Q_4 = \Delta\dot{\bar{\theta}}_j = \max(\dot{\bar{\theta}}_{j,k}) - \dot{\bar{\theta}}_{o\,j,k}$, where the subscript 'o' indicates its value just before impact. Such angular velocities of the inertial elements are calculated from the non-linear model. The severity of the impact is also evaluated by metric Q_5 which is the measure of maximum change in the relative kinetic energy between two inertial elements during an impact. Mathematically, Q_5 is defined below for the clearances AB and C (shown here by the superscripts) respectively:

$$Q_5^{AB} = \left|0.5J_A\dot{\bar{\theta}}_A^2\mathrm{sgn}(\dot{\bar{\theta}}_A) - 0.5J_B\dot{\bar{\theta}}_B^2\mathrm{sgn}(\dot{\bar{\theta}}_B)\right|,$$
$$Q_5^{C} = 0.5J_C\dot{\bar{\theta}}_C^2. \qquad (16a\text{-}b)$$

A closer look at the impulsive impacts (such as in Fig. 5c) reveals that each peak is followed by the ringing effect. As shown by Crowther et al. [18], the role of subsequent ringing could be reduced by using an exponentially decaying window over the duration of impact. Thus, a weighted mean square metric, Q_6, is defined to evaluate the intensity of the impact, given the following window:

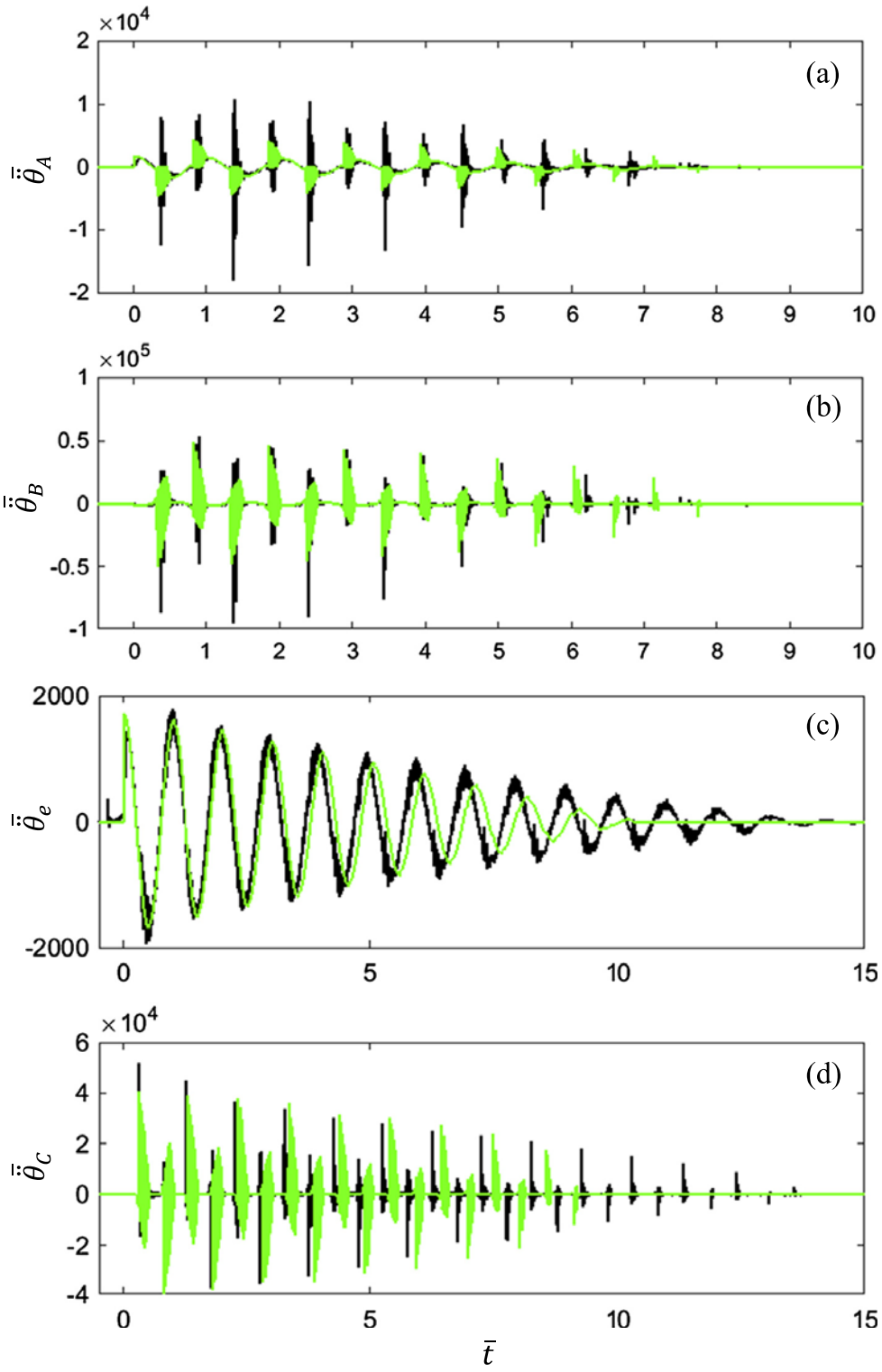

Fig. 7. Experimental validation of the non-linear models for two single clearance cases by comparing $\ddot{\bar{\theta}}(\bar{t})$ under step down torque ($\bar{T}$ = 1 to 0). (a) $\ddot{\bar{\theta}}_A(\bar{t})$ for Case II; (b) $\ddot{\bar{\theta}}_B(\bar{t})$ for Case II; (c) $\ddot{\bar{\theta}}_e(\bar{t})$ for Case III; and (d) $\ddot{\bar{\theta}}_C(\bar{t})$ for Case III. Key: (▬) – measured; and (▬) – predicted. Refer to Table 1 for the identification of the cases.

$$w_{Q_6} = \begin{cases} 0, & t < t_p \\ 1, & t_p \leqslant t < t_p + t_{w1} \\ e^{\varepsilon[t-(t_p+t_{w1})]} & t \geqslant t_p + t_{w1}. \end{cases} \tag{17}$$

Here, t_p is the point of impact. The length of step window, t_{w1}, is chosen so as to capture the portion of the response with the maximum amplitude. The decaying function is defined so that after a time interval of t_{w2}, only a 10% of the weighting is

Table 2
Comparison of measured and predicted (peak-peak) amplitudes of impulsive accelerations for dual and single clearance cases, defined in terms of Q_3 (dB re 1.0 rad/s^2).

Impact number	Measured at B	Predicted at B	Measured at C	Predicted at C
(a) Dual clearance configuration (Case V)				
1	100	96	98	95
	(97)[a]	(94)[a]	(101)[a]	(95)[a]
5	99	94	90	93
	(94)[a]	(92)[a]	(99)[a]	(93)[a]
9	92	91	88	90
	(77)[a]	(90)[a]	(84)[a]	(91)[a]

Impact number	Measured at B	Predicted at B		
(b) Single Clearance Configuration (Case IV)				
1	101	97	–	–
	(99)[a]	(95)[a]		
9	96	94	–	–
	(98)[a]	(93)[a]		
10	93	94	–	–
	(91)[a]	(92)[a]		

Key for
[a] Values reported in the prior paper by Krak and Singh [1].

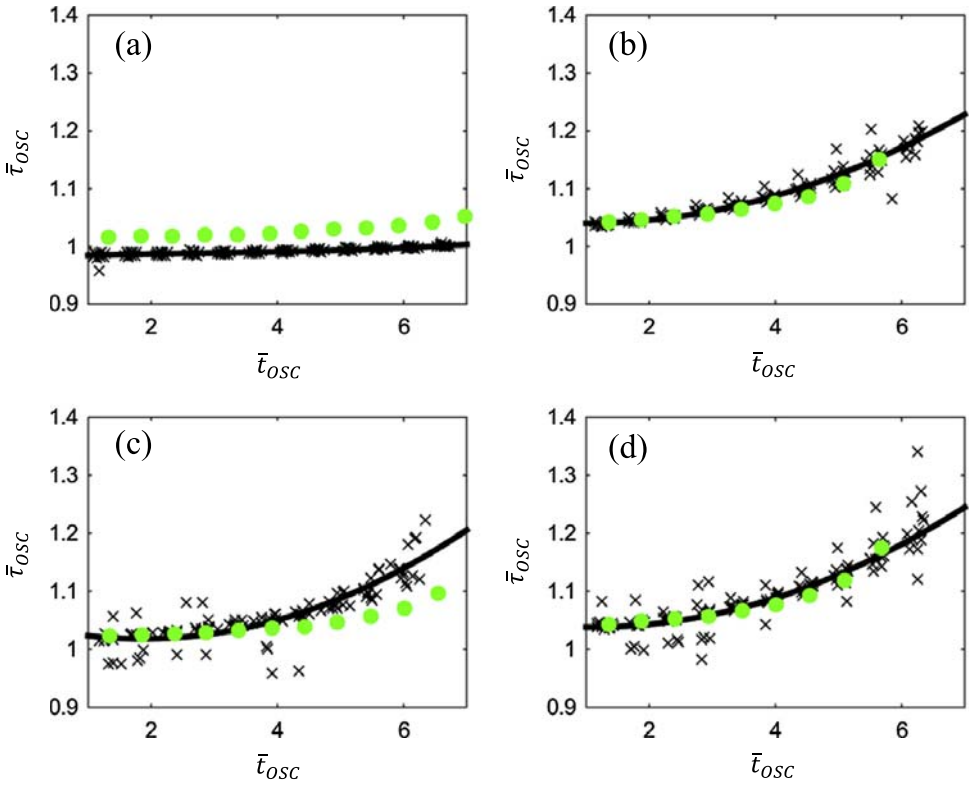

Fig. 8. Measured and predicted time varying periods for single and dual clearance cases under a step down torque ($\bar{T}$ = 1.0 to 0). (a) At the inertial element C for Case III; (b) inertial element B for Case II; (c) inertial element C for Case V; and (d) inertial element B for Case V. Key: (X) – measured value; (▬) – curve-fit of measured time periods; and (●) – predicted. Refer to Table 1 for the identification of the cases.

applied to the original signal. From this definition, the decay parameter comes out to be, $\varepsilon = \ln(0.1)/t_{w2}$. The metric Q_6 is calculated from the weighted signal, $\widehat{\ddot{\theta}}_j$ by using the following:

$$Q_6 = \frac{1}{t_{w1} + t_{w2}} \int_{t_k}^{t_k + t_{w1} + t_{w2}} \widehat{\ddot{\theta}}_j^2 dt. \tag{18}$$

The Q_6 metric is evaluated for only the first impact regime in both measured data and non-linear model predictions, for the acceleration signals from inertial elements B and C. Like Q_3, it again is converted to the logarithmic value by taking $10\log_{10}Q_6$, dB re 1.0 rad^2/s^4. Comparisons between the measured Q_3 (dB re 1.0 rad/s^2) and other metrics from predicted

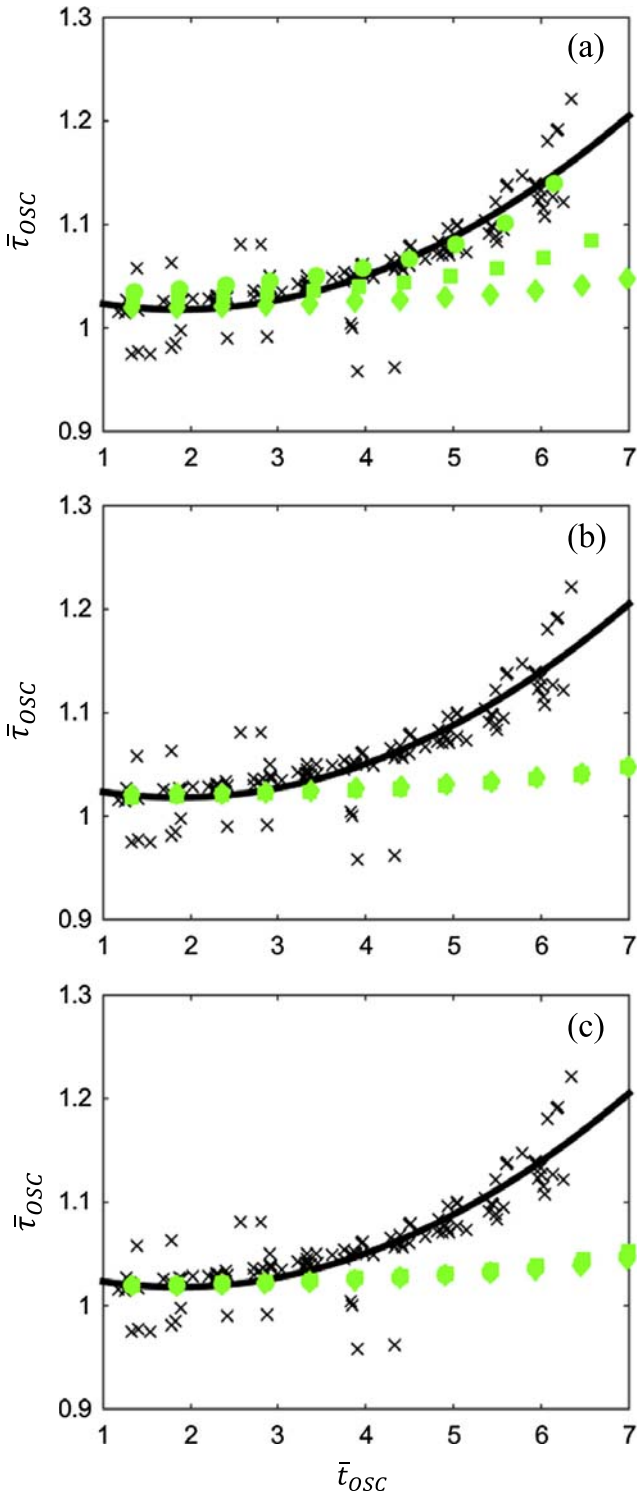

Fig. 9. Measured and predicted time varying periods for the single clearance configuration (Case II) at location B1 under a step down torque ($\bar{T}$ = 1.0 to 0), given a variation in key parameters of the non-linear model. (a) Variation in the clearance, with key: (●) – Θ_I; (■) – 1.5 Θ_I; and (◆) – 2 Θ_I; (b) variation in the stiffness with key: (●) – k_{AB}; (■) – 1.5k_{AB}; and (◆) – k_{AB}/1.5; and (c) variation in the hysteretic damping with key: (●) – h_{AB}; (■) – 1.5h_{AB}; and (◆) – h_{AB}/1.5. Key for all parts: (X) - measured; and (▬) - curve fit from measured time periods.

responses, such as Q_3, Q_4, Q_5 and Q_6 (dB re 1.0 rad^2/s^4), are shown in Fig. 10. Observe that higher peak-peak accelerations are usually associated with more changes in the relative kinetic energy and a larger change in the angular velocity. Measured and predicted values of two metrics, Q_1 and Q_6 (dB), are also compared in Table 3. A variation in Q_6 arises from the fact that it is an energy type metric (from the signal processing viewpoint). Lack of the Hertzian contact based stiffness and impact

damping formulations in the non-linear model might lead to inaccurate predictions of the peak acceleration amplitudes giving rise to some errors.

6. Linearized system analyses and comparison with non-linear model

The system of Fig. 1a is linearized to form Case I by assuming that the contact is always maintained in stage II for each clearance element ($k_A = k_C = k_{II}$). Regarding the dissipation, two formulations are used. First, the non-linear dry friction terms are linearized say over the first half period and step responses are analytically calculated using the initial value problem. Then an equivalent viscous damping matrix, **C**, is defined and its coefficients are found from the analytical step responses from the linearized dry friction formulation. Finally, the modal expansion method is used to calculate step responses and associated participation factors.

Recall that the Coulomb dry friction is defined via $\tanh(\sigma\dot{\theta})$ type expressions to reduce the computational difficulties. This term is replaced with $\mathrm{sgn}(\dot{\theta})$ and assumes that the motion is initiated only when the initial restoring force exceeds the static friction forces acting on the system. The linearized equations of motion for the system with constant hysteretic coefficients (h terms) for the 3DOF configuration, over the first half of the natural period is as follows; the direction of the velocity and friction reverse during the second half:

$$\begin{aligned} &J_A\bar{\ddot{\theta}}_A(\bar{t}) + k_{AB}\bar{\theta}_{AB}(\bar{t}) = h_{AB} + h_A,\\ &J_B\bar{\ddot{\theta}}_B(\bar{t}) - k_{AB}\bar{\theta}_{AB}(\bar{t}) + k_{BC}\bar{\theta}_{BC}(\bar{t}) = h_{BC} - h_{AB},\\ &J_C\bar{\ddot{\theta}}_C(\bar{t}) - k_{BC}\bar{\theta}_{BC}(\bar{t}) + k_C\bar{\theta}_C(\bar{t}) = h_C - h_{BC}. \end{aligned} \tag{19a-c}$$

The step down torque amplitude, T_{0+} at $t = 0+$ is converted to the initial displacement vector, $\boldsymbol{\theta}(0_+)$ for the system of Fig. 1a as:

$$\boldsymbol{\theta}(0_+) = \begin{Bmatrix} \Theta_C + \frac{T_0}{k_C} + \Theta_{BC} + \frac{T_0}{k_{BC}} + \Theta_{AB} + \frac{T_0}{k_{AB}} \\ \Theta_C + \frac{T_0}{k_C} + \Theta_{BC} + \frac{T_0}{k_{BC}} \\ \Theta_C + \frac{T_0}{k_C} \end{Bmatrix}. \tag{20}$$

The linear time-invariant (LTI) system is represented in matrix form as follows where 'diag' represents a diagonal matrix:

$$\mathbf{J}\ddot{\boldsymbol{\theta}}(\mathbf{t}) + \mathbf{K}\boldsymbol{\theta}(\mathbf{t}) = \mathbf{T}(\mathbf{t}), \tag{21}$$

$$\begin{aligned} &\mathrm{J} = \mathrm{diag}[J_A, J_B, J_C],\\ &\mathbf{K} = \begin{bmatrix} k_{AB} & -k_{AB} & 0 \\ -k_{AB} & k_{AB} + k_{BC} & -k_{BC} \\ 0 & -k_{BC} & k_{BC} + k_C \end{bmatrix},\\ &\mathbf{T}(t) = [h_A + h_{AB}h_{BC} - h_{AB}h_C - h_{BC}]^T,\\ &\boldsymbol{\theta}(t) = [\theta_A(t)\ \theta_B(t)\ \theta_C(t)]^T. \end{aligned} \tag{22a-d}$$

The eigenvalue matrix, $\boldsymbol{\Lambda}$, of the undamped system is determined from the characteristic equation, $|\mathbf{J}^{-1}\mathbf{K} - \boldsymbol{\Lambda}\mathbf{I}| = 0$; $\boldsymbol{\Lambda} = \mathrm{diag}(\lambda_r); r \in \{1, 2, 3\}$, where $\lambda_r = \omega_r^2$, and r is the modal index. The three natural frequencies (ω_r) are found to be 93 rad/s (14.8 Hz), 4661 rad/s (742 Hz) and 4840 rad/s (770 Hz) respectively. The eigenvector matrix **U** satisfies this expression: $[\mathbf{J}^{-1}\mathbf{K} - \boldsymbol{\Lambda}\mathbf{I}]\mathbf{U} = 0$. The three modes of the system (when normalized to yield unity modal mass values) are as follows where the superscript T is the transpose of the vector: $\mathbf{U}_2 = [13.5\ 13.5\ 0.075]^{\mathrm{T}}$; $\mathbf{U}_2 = [0.3\ -3.3\ -50]^{\mathrm{T}}$; and $\mathbf{U}_3 = [3.8\ -48\ 3.4]^{\mathrm{T}}$. For further analysis, these modes are re-normalized where each modal term is divided by the highest element in its respective column and then approximated (identified by the 'hat' on **U**) to the nearest whole number to yield the following eigenvectors: $\hat{\mathbf{U}}_1 = [1\ 1\ 0]^{\mathrm{T}}$; $\hat{\mathbf{U}}_2 = [0\ 0\ 1]^{\mathrm{T}}$; and $\hat{\mathbf{U}}_3 = [0\ 1\ 0]^{\mathrm{T}}$.

The undamped equations of motion, as defined by Eq. (19), are converted into the modal (normal) coordinates $\boldsymbol{\eta} = \mathbf{U}\boldsymbol{\theta}$ to yield the following uncoupled equations where the modal torque vector is $\mathbf{N} = \mathbf{U}^{\mathrm{T}}\mathbf{T}$:

$$\ddot{\boldsymbol{\eta}}(t) + \boldsymbol{\Lambda}\boldsymbol{\eta}(t) = \mathbf{N}(t). \tag{23}$$

Further, the initial displacement vector in the modal domain is $\boldsymbol{\eta}(0) = \mathbf{U}^{\mathrm{T}}\mathbf{J}\boldsymbol{\theta}(0)$. Given the numerical values, the initial conditions in normal coordinates are: $\eta_1(0) = 0.00573$, $\eta_2(0) = 8.2 \times 10^{-6}\ \eta_1(0)$ and $1 \times 10^{-4}\ \eta_1(0)$. The undamped displacement response for mode r is obtained as:

$$\eta_r(t) = \left(\eta_r(0) - \frac{\mathrm{N}_r}{\omega_r^2}\right)\cos\omega_r t + \frac{\mathrm{N}_r}{\omega_r^2}. \tag{24}$$

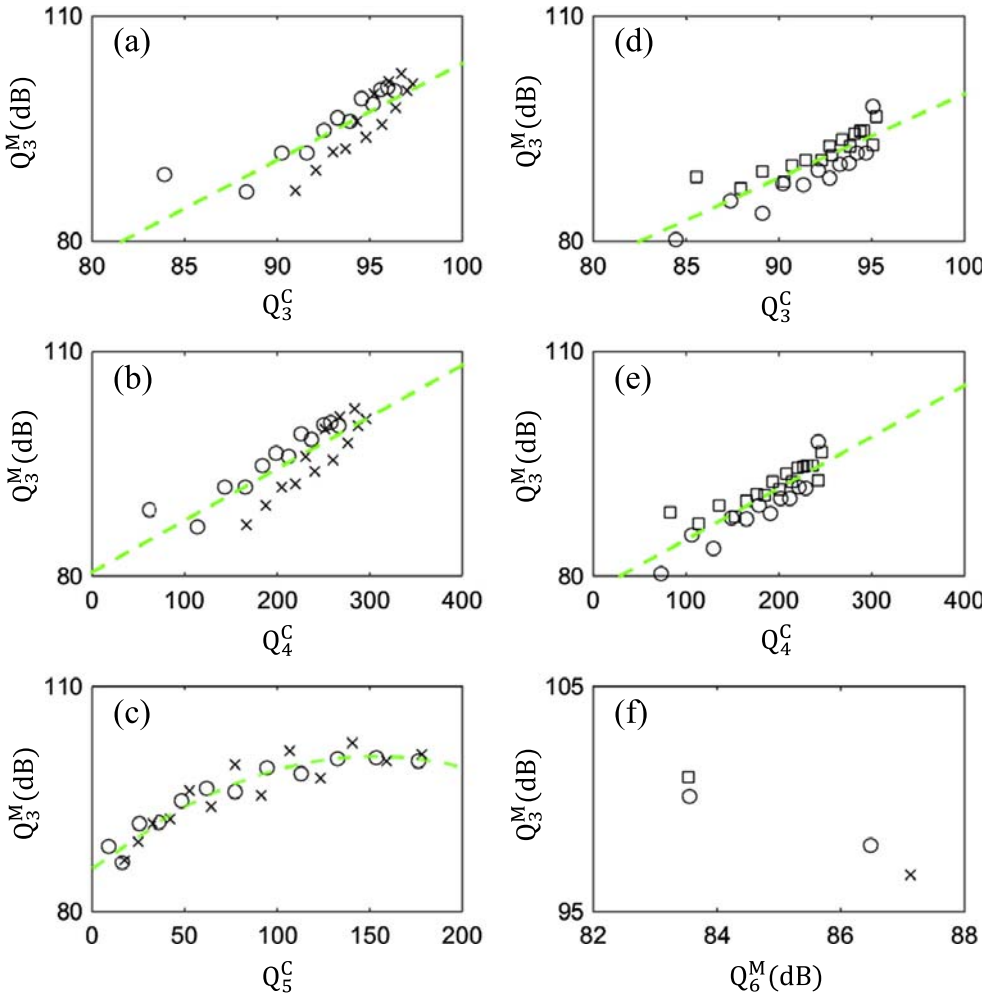

Fig. 10. Comparative assessment of the metrics for the single and dual clearance cases, evaluated at inertial locations B and C under step down torque ($\bar{T}$ = 1.0 to 0) where superscripts M and C denote measured and predicted values respectively. The first column corresponds to location B and the second column corresponds to location C. The references for dB values are re 1.0 rad/s^2 for Q_3 and 1.0 rad^2/s^4 for Q_6. (a) Measured Q_3 vs. predicted Q_3 at B; (b) measured Q_3 vs. predicted Q_4 at B; (c) measured Q_3 vs. predicted Q_5 at B; (d) measured Q_3 vs. predicted Q_4 at C; (e) measured Q_3 vs. predicted Q_4 at C; and (f) measured Q_3 vs. measured Q_6. Key: (---) – curve-fit of single and dual clearance values; (X) – Case III; (□) – Case V; and (O) – Case II. Refer to Table 1 and Fig. 2 for the identification of cases and locations respectively.

Table 3
Measured and predicted values of metrics Q_1 (number of impacts) and Q_6 (time windowed mean-square angular acceleration, in dB re 1.0 rad^2/s^4) evaluated for single and dual clearance cases. Values reported under the single clearance case at location B are from Case II and at location C are from Case III.

Metric	Location	Single clearance case (II or III)		Dual clearance case (V)	
		Predicted	Measured	Predicted	Measured
Q_1	B	16	15	12	16
	C	18	27	12	15
Q_6	B	84	87	83	87
	C	83	84	82	84

The peak modal displacement, for the linearized dry friction case, at the end of the first natural period ($\tau_1 = 2\pi/\omega_1$ when $\dot{\eta}_r(t) = 0$) is $\eta_1(t_1) = -(\eta_1(0) - \frac{4N_1}{\omega_1^2})$. Assuming the system to be now viscously damped, Eq. (24) is modified to yield the following response at mode r:

$$\theta_r(t) = \eta_r(0)e^{-\varsigma_r\omega_r(t)}(\cos(\omega_{rd}t) + \frac{\varsigma_r}{\sqrt{1-\varsigma_r^2}}\sin(\omega_{rd}t)). \tag{25}$$

Here, ς_r is the modal damping ratio and $\omega_{rd} = \omega_r\sqrt{1-\varsigma_r^2}$ is the damped natural frequency. By equating Eqs. (25) and (24) at time $t = \tau_1$, the equivalent viscous damping ratios of the linear system are found to be: ς_1 = 0.011, ς_2 = 0.590, ς_3 = 0.151. The corresponding modal viscous damping matrix is: $\mathbf{C}_m = \text{diag}[2\varsigma_r\omega_r]$ and it is constructed as: $\mathbf{C} = (\mathbf{U}^T)^{-1}\mathbf{C}_m\mathbf{U}^{-1}$.

Similar to the simplifications used for Case V (3DOF system), the governing equations of the two single clearance configurations, Case II (Eq. (11)) and Case III (Eq. (12)) can be linearized and simplified as 2DOF systems. Their approximated eigenvectors for the first mode are: $\hat{\mathbf{U}}_1 = [1\ 1]^T$ for Case II and $\hat{\mathbf{U}}_1 = [1\ 0]^T$ for Case III. It is interesting to note that the eigenvectors of the linearized Case II and III are found to be subsets of the eigenvector for linearized Case V though the experimental system was not designed as such [1]. The time domain (step) responses calculated via the modal superposition method are compared with the non-linear model response in Fig. 11 only for Case V (without the clearances but with non-linear dry friction terms). As expected, the response is dominated by the first mode. Overall, an excellent match between the linear and non-linear models are found at lower values of $\bar{\tau}$ (say up to $\bar{t}$ = 7) since the equivalent viscous damping ratios have been approximated from step responses over the first time period only. Comparisons for the single clearance configurations can also be easily derived with the same procedure.

Predicted accelerations between the non-linear and linear models for Case V are compared in Fig. 12. Ignoring the impulsive peaks (that occur due to the transitions at clearances), the responses from the linear model match closely with the low frequency sinusoid from the non-linear model say for the first two time periods. Denoting the maximum acceleration (of the lower frequency sinusoid just after impact) for the j^{th} inertial element as P_j, the elements of amplitude ratio vector, **R**, after any particular impact is defined for the 3DOF configuration as follows:

$$\mathbf{R} = \left[\frac{P_A}{P_A}\ \frac{P_B}{P_A}\ \frac{P_C}{P_A}\right]^T. \tag{26}$$

Similar definitions are used for the 2DOF configurations. The value of **R** (similar to the operating motion survey type vector in the linear system dynamics) after the second impact is predicted to be as follows for Cases V, II and III: $[1\ 0.97\ 0.24]^T$, $[1\ 1]^T$ and $[1\ 0]^T$ respectively. Since only the peak of low frequency sinusoid is considered, the magnitudes of harmonic accelerations directly correlate with the magnitude of harmonic displacements. Therefore, **R** values represent the relative displacements between the inertias (under the impulsive conditions though). They are now compared with the calculated linear system eigenvectors at the first mode. Comparing **R** to $\hat{\mathbf{U}}_1$, a close match in the values is observed; for example, $\mathbf{R} = [1\ 0.97\ 0.24]^T$ and $\hat{\mathbf{U}}_1 = [1\ 1\ 0]^T$ for Case V. This confirms that the displacement patterns of the non-linear system follow

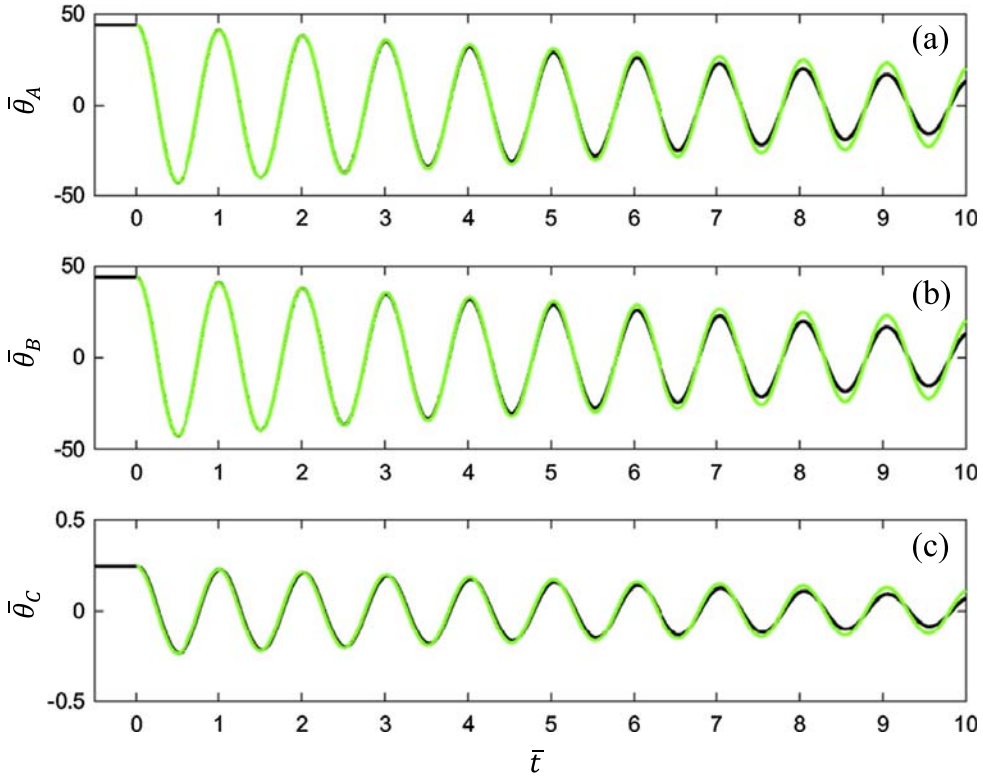

Fig. 11. Comparison between 3DOF non-linear and linear system models for the linearized system (Case V and I) under step down torque ($\bar{T}$ = 1.0 to 0). (a) $\bar{\theta}_A(\bar{t})$; (b) $\bar{\theta}_B(\bar{t})$; and (c) $\bar{\theta}_C(\bar{t})$. Key: (▬) – non-linear model (Case V without two clearances but including dry friction elements); and (▬) – linear model (Case I with effective viscous damping elements and linear stiffness elements).

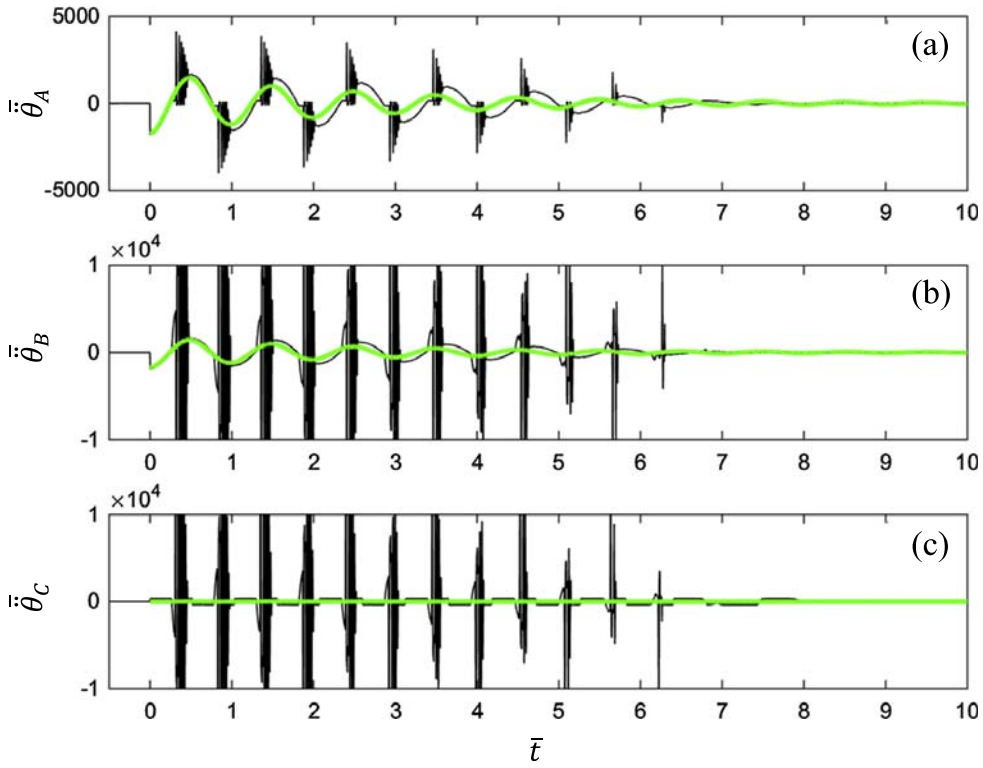

Fig. 12. Comparison between 3DOF non-linear and linear system models for the dual clearance configuration (Case V) under step down torque ($\bar{T}$ = 1.0 to 0). (a)$\ddot{\bar{\theta}}_A(\bar{t})$; (b)$\ddot{\bar{\theta}}_B(\bar{t})$; and (c) $\ddot{\bar{\theta}}_C(\bar{t})$. Key: (——) – non-linear model (Case V with clearance and friction elements); and (——) – linear model (Case I with viscous damping).

the mode shapes calculated using the analogous linear systems. Similar observations are found for Cases II and III as $\mathbf{R} = [1\ 1]^T$ and $[1\ 0]^T$ match perfectly with the corresponding eigenvectors $\hat{\mathbf{U}}_1 = [1\ 1]^T$ and $\hat{\mathbf{U}}_1 = [1\ 0]^T$ respectively. These observations suggest that the non-linear system retains some intrinsic properties of the underlying linear system.

7. Comparisons between dual clearance configurations

Two additional dual clearance configurations, namely Cases IV and VI of Table 1, are computationally investigated and compared with Case V that has been comprehensively examined thus far using experimental and computational methods. First, consider the following governing equations for Case IV that has the clearances at BC and C and a compliant linear spring at AB:

$$\begin{aligned} &J_A\ddot{\bar{\theta}}_A + \Psi_A(\dot{\bar{\theta}}_A) + \Psi_{AB}(\dot{\bar{\theta}}_{AB}) + k_{AB}(\bar{\theta}_{AB}) = \bar{T}(\bar{t}),\\ &J_B\ddot{\bar{\theta}}_B - \Psi_{AB}(\dot{\bar{\theta}}_{AB}) + \Psi_{BC}(\dot{\bar{\theta}}_{BC}) - k_{AB}(\bar{\theta}_{AB}) + \Phi_{BC}(\bar{\theta}_{BC}) = 0,\\ &J_C\ddot{\bar{\theta}}_C - \Psi_{BC}(\dot{\bar{\theta}}_{BC}) + \Psi_C(\dot{\bar{\theta}}_C) - \Phi_{BC}(\bar{\theta}_{BC}) + \Phi_C(\bar{\theta}_C) = 0. \end{aligned} \tag{27a-c}$$

Similarly, the governing equations of Case VI that has clearances at AB and BC and a compliant linear spring at C are:

$$\begin{aligned} &J_A\ddot{\bar{\theta}}_A + \Psi_A(\dot{\bar{\theta}}_A) + \Psi_{AB}(\dot{\bar{\theta}}_{AB}) + \Phi_{AB}(\bar{\theta}_{AB}) = \bar{T}(\bar{t}),\\ &J_B\ddot{\bar{\theta}}_B - \Psi_{AB}(\dot{\bar{\theta}}_{AB}) + \Psi_{BC}(\dot{\bar{\theta}}_{BC}) - \Phi_{AB}(\bar{\theta}_{AB}) + \Phi_{BC}(\bar{\theta}_{BC}) = 0,\\ &J_C\ddot{\bar{\theta}}_C - \Psi_{BC}(\dot{\bar{\theta}}_{BC}) + \Psi_C(\dot{\bar{\theta}}_C) - \Phi_{BC}(\bar{\theta}_{BC}) + k_C(\bar{\theta}_C) = 0. \end{aligned} \tag{28a-c}$$

The dominating first eigenvector for the linearized 3DOF system of each configuration is: $\mathbf{U}_1 = [14.1\ 0.16\ 0.08]^T$ for Case IV and $\mathbf{U}_1 = [13.1\ 13.0\ 12.9]^T$ for Case VI. Each eigenvector is re-normalized and approximated to the nearest whole number to yield: $\hat{\mathbf{U}}_1 = [1\ 0\ 0]^T$ for Case IV and $[1\ 1\ 1]^T$ for Case VI. The non-linear model is then used to predict the responses of both configurations under a step down torque from $\bar{T}$ = 1.0 to 0. Figs. 13 and 14 compare responses of the original experimental system (Case V) and two additional dual clearance configurations (Cases VI and IV) respectively. Like the previous section, the amplitude ratio vector **R** is again evaluated and compared with the dominant first eigenvectors for Cases IV and VI. These are found to be: $\mathbf{R}\ [1\ 0\ 0]^T$ for Case IV and $\mathbf{R}\ [1\ 1\ 1]^T$ for Case VI; these perfectly match the first eigenvector $\hat{\mathbf{U}}_1$ calculated from their respective linearized systems.

The Q_3 values (in dB re 1.0 rad/s^2) of the first impact at J_B and J_C for Case IV (Fig. 14b and c respectively) are 97 dB and 98 dB respectively and 12 impacts (Q_1) are seen at both inertias. Observe that no impacts occur at J_A in Case IV (Fig. 14a). Similarly, the Q_3 values of the first impact at J_A,J_B and J_C for Case VI are 72 dB, 95 dB and 92 dB respectively and all three

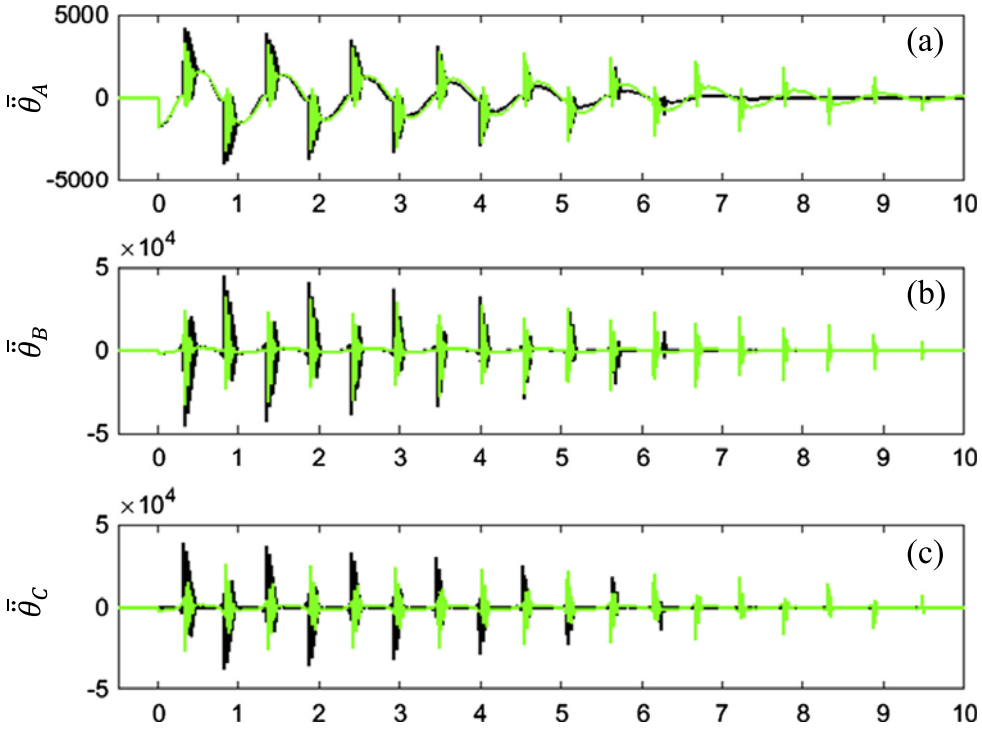

Fig. 13. Comparison of responses between alternate dual clearance configurations (Cases V and VI) cases under step down torque ($\bar{T}$ = 1.0 to 0). (a) $\ddot{\bar{\theta}}_A(\bar{t})$; (b) $\ddot{\bar{\theta}}_B(\bar{t})$; and (c) $\ddot{\bar{\theta}}_C(\bar{t})$. Key: (▬) – Case V; and (▬) – Case VI. Refer to Table 1 for identification of these cases.

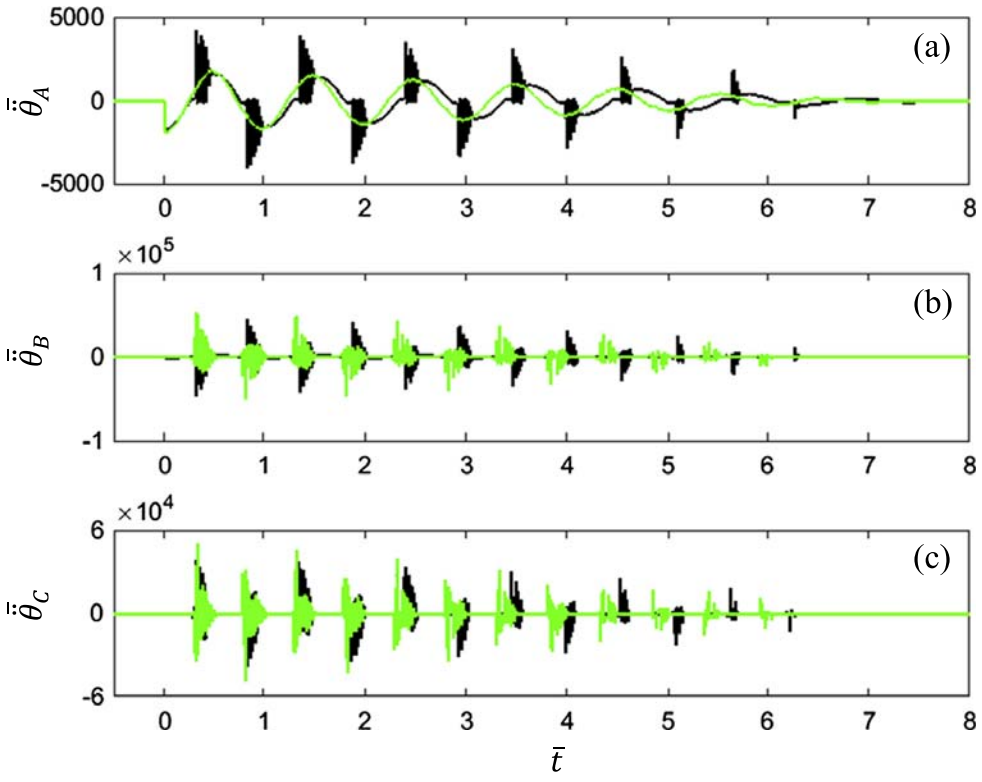

Fig. 14. Comparison of step responses between alternate dual clearance configurations (Cases IV and V) under step down torque ($\bar{T}$ = 1.0 to 0). (a) $\ddot{\bar{\theta}}_A(\bar{t})$; (b) $\ddot{\bar{\theta}}_B(\bar{t})$; and (c) $\ddot{\bar{\theta}}_C(\bar{t})$. Key: (▬) – Case IV; and (▬) – Case V. Refer to Table 1 for identification of the cases.

inertias see 18 impacts. The magnitudes of the first impact at J_C for Case VI are 3 dB lower (and 3 dB higher in Case IV) when compared with corresponding values in Case V. The number of impacts in Case VI is higher than in Case V possibly due a reduction in the kinetic energy per impact at J_C. The relative angular displacement at the clearances for both Cases IV and VI (not shown for the sake of brevity) confirm that all impacts are dual sided in nature.

The time periods of impacts are compared in Fig. 15 for three dual clearance configurations and each case shows a softening trend. In particular $\bar{\tau}_{osc}(\bar{t}_{osc})$ results for Case VI exhibit somewhat of a linear system response over several time periods when compared with Cases IV and V. Observe how closely the time periods for the three inertial elements overlap for Case VI indicating that this system essentially behaves more like a SDOF non-linear system which is reinforced by the eigenvector ($\hat{\mathbf{U}}_1$) of the corresponding linearized system.

8. Effect of step excitation profile and amplitude on non-linear responses

The validated non-linear simulation model is used to first examine the effect of step-like excitation (or the shape of torque profile) that is simulated by an exponentially decaying excitation as defined by Eq. (6) since it is of particular significance in controlling the clunk like events in vehicles [19]. As the value of parameter β is asymptotically reduced, this would approach the ideal step input given by Eq. (5). For a higher value of β, predicted amplitude(s) and number of impact(s) reduce for Cases II, III and V. Fig. 16 compares typical responses for an ideal step down input from $\bar{T}$ = 1.0 to 0 and a comparable exponentially decaying excitation with β = 0.15. Key results for Case V are summarized in Table 4. Observe that the peak-peak amplitudes diminish more rapidly under an exponential decaying input as β is increased; again only a softening trend is observed in their time periods.

The non-linear model is next utilized to examine the influence of excitation amplitude (step height of $\bar{T}$) on the single and dual clearance configurations (namely Case II and V respectively). By using Eq. (5), both ideal step down and step up excitations are examined by varying the values of initial and final torques. It is observed that a step function with a higher step height leads to an increased peak-peak impulsive amplitude. For those excitations that begin from $\bar{T}_0$ = 0, the model predicts

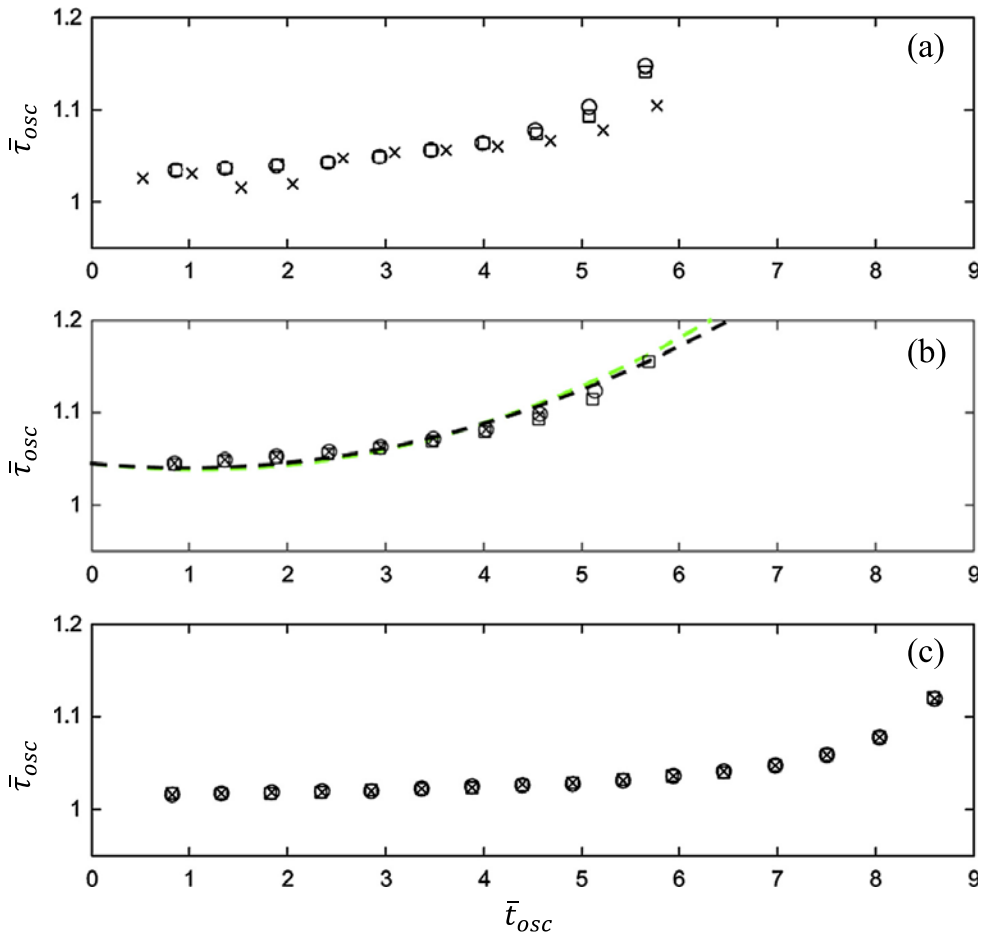

Fig. 15. Predicted and measured time varying periods for three dual clearance configurations (Cases IV, V and VI) under a step down torque ($\bar{T}$ = 1.0 to 0) cases. (a) Case IV; (b) curve fit of measured data for Case V with key: (---) – at location B; and (—) – at location C; and (c) Case VI. Key for all parts: (X) – J_A; (O) – J_B; and (□) – J_C. Refer to Table 1 and Fig. 1 for the identification of cases and locations respectively.

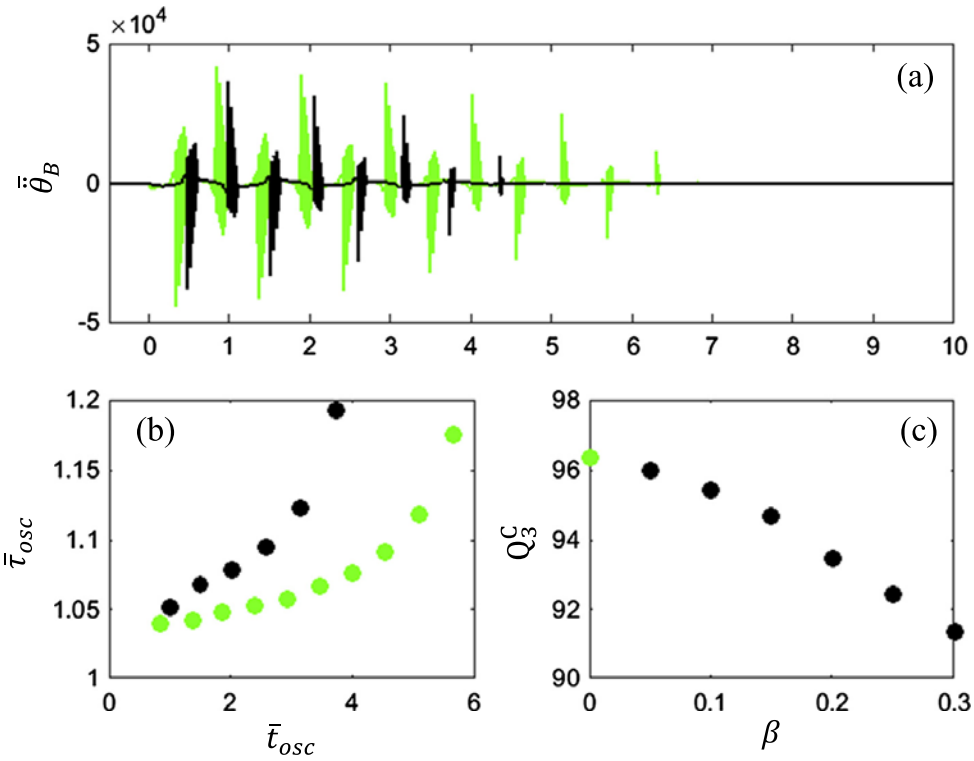

Fig. 16. Comparison of responses between ideal step down and step like exponential torques applied to the dual clearance configuration (Case V at inertial location B). (a) Exponentially decaying torque, with key: (—) – step function; and (—) – exponentially function; (b) time periods $\bar{\tau}_{osc}(\bar{t})$; and (c) predicted Q3 vs. β relations. Key for parts (b) and (c): (●) – step down torque; and (X) – exponentially decaying torque.

Table 4
Effect of the step input profile and amplitude on the responses. All values shown are the predictions at location B (and the Q effective inertial location for Case VII). The Q_3 values (dB re 1.0 rad/s^2) are only for the first impact. Refer to Table 1 and Fig. 1 for the identification of cases.

Input torque	$\bar{T}_0$	$\bar{T}_f$	Case	Number of clearances	Q_3 (dB)	Q_1	Trends in $\bar{\tau}_{osc}$ (nature of impacts)
Exponential step down (Eq. (6))	1	0	V	2	96 (β = 0.05)	12	Softening (di)
					94 (β = 0.15)	8	Softening (di)
					92 (β = 0.3)	4	Softening (di)
Step down (Eq. (5))	1	−1	II	1	101	20	Softening (di)
			V	2	100	16	Softening (di)
			VII	1	36	16	Hardening (si)
			VIII	3	65	12	Hardening (di & si)
Step up (Eq. (5))	−1	2	II	1	102	20	Softening (di)
			V	2	102	16	Softening (di)
			VII	1	39	21	Hardening (si)
			VIII	3	69	15	Hardening (di & si)

Key to the nature of impacts is: di is for the double sided impacts and si is for the single sided impact.

only one impact as there is no initial restoring force in the system. In fact, for this case the $\bar{\theta}_{ij}$ at the clearances shows that only one transition is crossed between the stages (II and I of Fig. 1b). Note that $\bar{T}_0 = 0$ is not used for normalization of any results.

In addition, two other configurations (Cases VII and VIII as listed in Table 1) are formulated to better understand the vibro-impact phenomena. Case VII considers an effective SDOF system with one clearance and thus will be compared with Case II (3DOF system with a single clearance at AB). Case VIII goes back to the generic 3DOF system formulation of Fig. 1a with 3 clearances; it will be compared with the experimental dual clearance configuration (Case V) under several step input profiles. The clearance introduced at BC is similar to the clearance at C (0.1°) while the clearance at AB (0.15°) is unchanged. Since the linearized system dynamics suggests that the step response is dominated by the first mode, an effective (with 'eff' subscript) non-linear SDOF system (Case VII, as a subset of Fig. 1a) with one clearance element (k_{AB}) and two dry friction elements (h_A and h_{AB}) is developed as:

$$J_{eff}\ddot{\bar{\theta}}_{eff} + \Psi_{AB}(\dot{\bar{\theta}}_{eff}) + \Psi_A(\dot{\bar{\theta}}_{eff}) + k_{BC}\bar{\theta}_{eff} + \Phi_{AB}(\bar{\theta}_{eff}) = \bar{T}(\bar{t}) \tag{29}$$

The effective inertia J_{eff} is chosen so that it matches the first natural frequency of the linearized torsional system with no clearances (Case I). An alternate configuration of Case VII can be constructed by deleting the linear stiffness k_{BC} but the non-linear step responses are identical with or without the k_{BC} term. Thus results are given here for the system that does not include the linear k_{BC} term. However, only one impact is seen in this SDOF system (Case VII) for a step down torque from $\bar{T}$ = 1.0 to 0. The stage transition Θ_l is crossed only once and the inertial element stays within the gap; an absence of a restoring torque in the SDOF system (even with a linear k_{BC} element) induces this type of behavior, unlike other configurations (such as Case II and V).

Next, the step excitation amplitude is changed to $\bar{T}$ = 1.0 to −1.0 to ensure that the final (end) point is outside the gap regime. Non-linear step responses for Cases II, III and V show that the peak-peak acceleration amplitudes increase and the time histories are now longer than those predicted previously under the $\bar{T}$ = 1.0 to 0 amplitude. For the sake of illustration, results between these two step amplitudes for Case V are compared in Fig. 17. Over the first five impacts, an increase of about 4 dB is noticed in Q_3. The time periods ($\bar{\tau}_{osc} \approx 1$) are closer to the first natural time period of the linearized configuration (Case I) as shown in Fig. 17b. Observe that the spacing between the stage transitions (Fig. 17c) changes with a higher step height. The impacts at Θ_l motions against the direction of the final torque $\bar{T}$ = −1.0) occur more rapidly when compared to the predictions with the zero final torque. Fig. 17d illustrates that the dynamic torque through the clearance AB is higher than the one seen previously with lower torque amplitude.

The final 3DOF configuration with three concurrent clearances (Case VIII) is studied next; note that this system is stiffer than the configurations considered before (such as Case V). The natural frequencies of the corresponding linearized system are calculated to be 117 Hz, 755 Hz and 1285 Hz which are higher than the ones found before (14.8 Hz, 742 Hz and 770 Hz) since a compliant spring is no longer used here. Accordingly, the first natural time period of 8.5 ms is used to normalize the time and motion variables of Case VIII unlike the rest of the configurations where a time period of 67 ms corresponding to a simplified linear SDOF configuration (Eq. (7)) has been used.

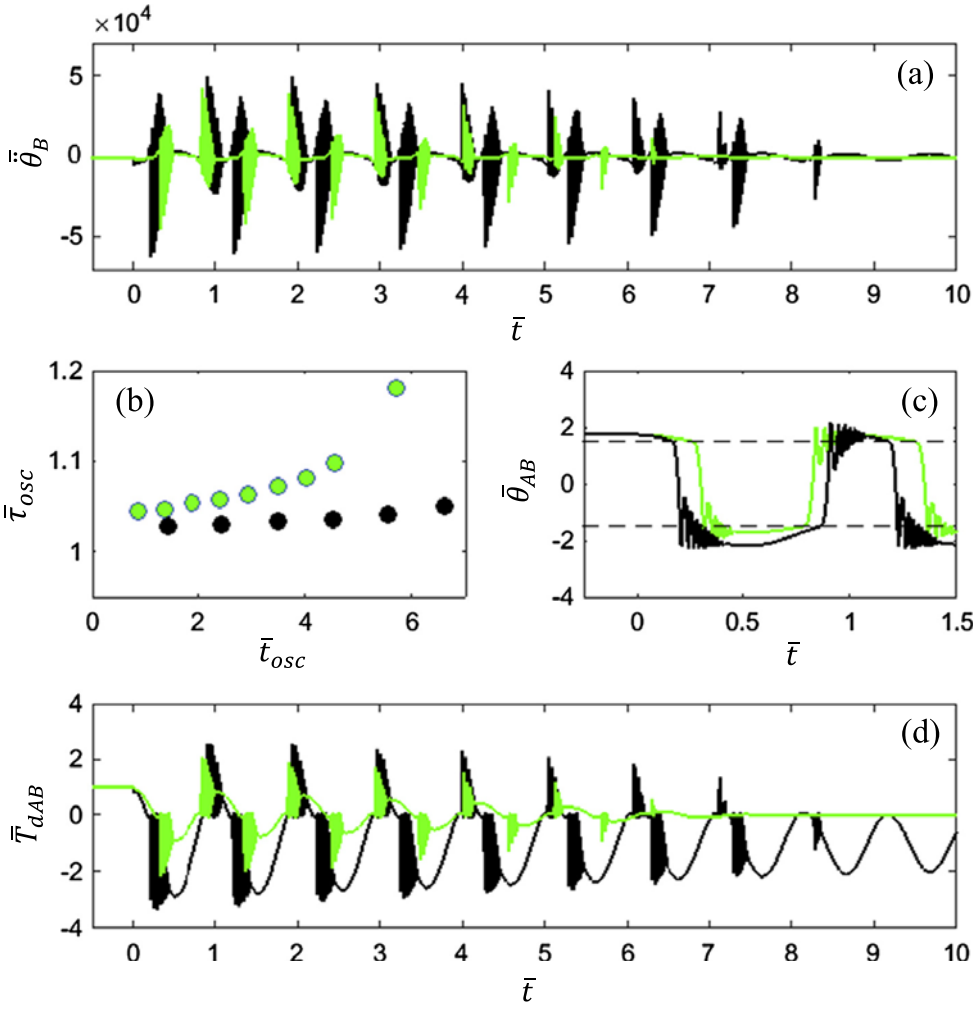

Fig. 17. Effect of the step excitation amplitude on responses for the dual clearance configuration (Case V); here two step down torque inputs are considered (from $\bar{T}$ = 1.0 to 0 and from $\bar{T}$ = 1.0 to −1.0). (a) $\bar{\ddot{\theta}}_{AB}(\bar{t})$ vs. $\bar{\theta}_{AB}(\bar{t})$, with key: (▬) – from $\bar{T}$ = 1.0 to 0; and (▬) – from $\bar{T}$ = 1.0 to −1.0; (b) $\bar{\tau}_{osc}$ vs. $\bar{t}_{osc}$, with key: (●) – from $\bar{T}$ = 1.0 to 0; and (●) – from $\bar{T}$ = 1.0 to −1.0; (c) $\bar{\theta}_{AB}$ vs. $\bar{t}$; and (d) $\bar{T}_{dAB}(\bar{t})$. Key: (▬) – from $\bar{T}$ = 1.0 to 0; and (▬) – from $\bar{T}$ = 1.0 to −1.0.

Typical non-linear responses are compared in Fig. 18 for Case II vs. Case VII and Case V vs. Case VIII under a step down torque from $\bar{T}$ = 1.0 to −1.0. The same results are found for a step up from $\bar{T}$ = −1.0 to 1.0 though with a reversal in the direction of motion. Observe that Cases VII and VIII show lower peak-peak acceleration amplitudes when compared to Cases II and V in Fig. 18b and c respectively. Unlike the softening trend that has been observed in $\bar{\tau}_{osc}(\bar{t}_{osc})$ for Cases II and V, Cases VII and VIII exhibit the hardening behavior as shown in Fig. 18d and e with time periods starting from around 2 showing a period doubling effect (and not close to the starting value of 1 as previously seen) though it reduces to unity with time. The relative angular displacement time history for Case VII indicates that only single sided impacts are seen here; the phase plane plot confirms this although lower angular velocities are found when compared to Case II. In contrast, a transition from the double sided to single sided impacts is seen for Case VIII, leading to the no impact regime gradually. The phase plane plot for this configuration shows a minor chaotic behavior (Fig. 18a) unlike other seven configurations of Table 1 where no evidence of chaos has been found. Issues related to bifurcations under transient loading with one or more clearances have not been examined unlike previous research on the bifurcation of an impacting oscillator under harmonic excitation [38,39].

When the step torque amplitude is increased from $\bar{T}$ = −1.0 to 2.0, higher peak-peak acceleration amplitudes and longer time histories are found for all configurations. In particular, the values of $\bar{\tau}_{osc}(\bar{t}_{osc})$ tend to reduce and the non-linear system seems to be now 'saturated'. It seems to behave more as a linear system with an increase in the step height since the inertial elements now stay in the contact (positive stiffness) regimes. The phase plane plots, however, are similar to the previous cases though higher angular velocities are seen. The effect of $\bar{T}(\bar{t})$ on Q_3 values (in dB re 1.0 rad/s^2) and accompanying trends (such as softening or hardening) are summarized in Table 4. For a step excitation where $\bar{T}_0 \neq 0$ and $|\bar{T}_f| > |\bar{T}_0|$, the initial and final operating points lie within the same stage of the static $k_{ij}(\theta_{ij})$ curve; hence there are no stage transitions and consequently no impacts are generated.

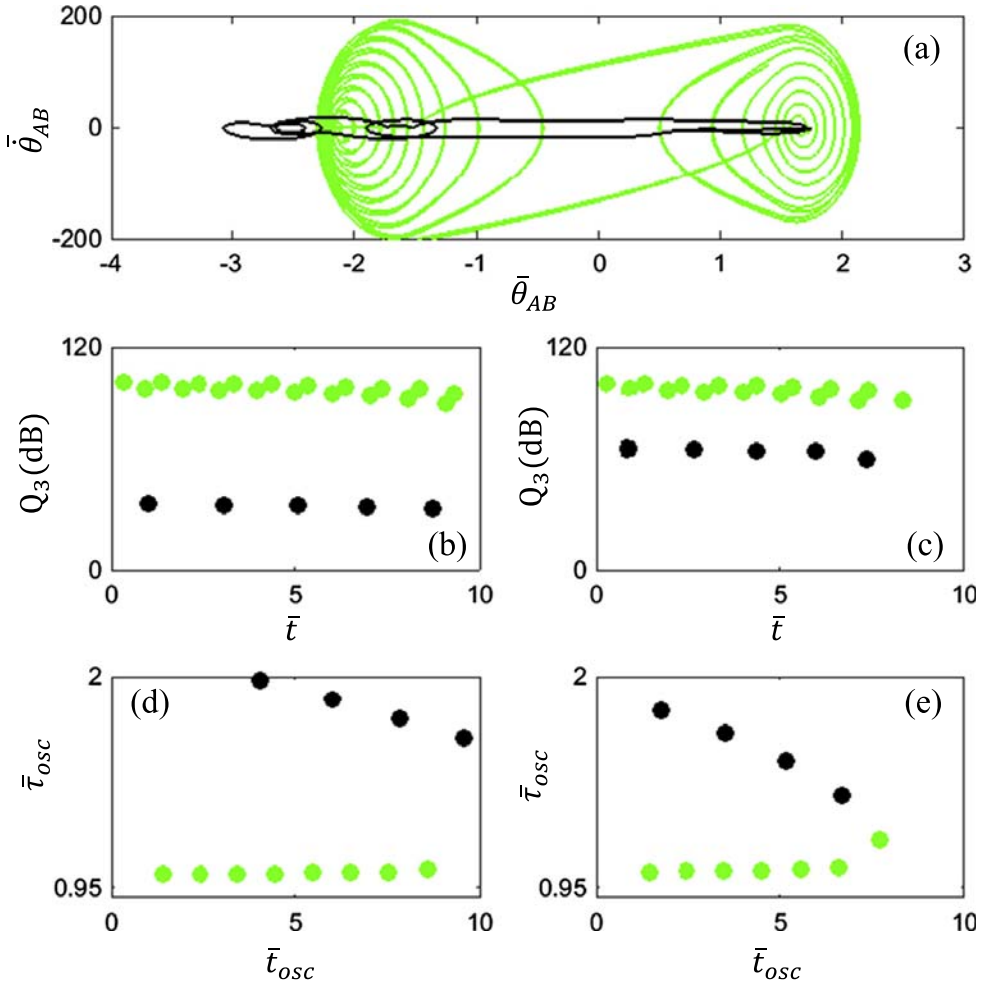

Fig. 18. Comparison of non-linear step responses (at location B) between Cases II and VII (each with a single clearance) and between Cases V (with two clearances) and VIII (with three clearances) to a step down torque from ($\bar{T}$ = 1.0 to −1.0). (a) $\dot{\bar{\theta}}_{AB}(\bar{t})$ vs. $\bar{\theta}_{AB}(\bar{t})$ from $\bar{t}$ = 0 to 2.0, with key: (▬) – Case V; and (▬) – Case VIII; (b) Q3 vs. $\bar{t}$ with key: (●) – Case II; and (●) – Case VII; (c) Q3 vs. $\bar{t}$, with key: (●) – Case V; and (●) – Case VIII; (d) $\bar{\tau}_{osc}(\bar{t}_{osc})$, with key: (●) – Case II; (●) – Case VII; and (e) $\bar{\tau}_{osc}(\bar{t}_{osc})$, with key: (●) – Case V; (●) – Case VIII. Refer to Table 1 for more details on the four configurations compared here.

Finally, the Fourier transforms of the accelerations (at the effective inertial locations) are calculated (though not shown here for the sake of brevity) given a step down torque from $\bar{T}$ = 1.0 to −1.0. These estimations are made using the entire time record (with Hamming window) with 2000 Hz as the upper frequency limit and a frequency resolution of 0.4 Hz. The spectral magnitudes are found to be much lower for Cases VII and VIII when compared to Cases II and V respectively. Dominant peak is located at 20 Hz for Case VII which is close to the natural frequency of a linear SDOF system (15 Hz). Peaks for Case II are observed at 15 Hz and at 750 Hz (again close to the natural frequencies). Fourier transform of Case VIII indicates that the higher modes are being excited, with peaks around 800 Hz and 1400 Hz (close to the natural frequencies); conversely, whereas peaks are observed only around 750 Hz in Case V. No peaks at the lower frequencies (<100 Hz) are found for Case VIII possibly due to higher eigenvalues.

9. Conclusion

This article significantly extends prior research by re-acquiring detailed measurements on the scientific experiment [1] with a higher sampling frequency and by placing additional sensors. Also, the non-linear formulation has been generalized to include one, two or three clearances (along with dry friction elements) and their step responses have been examined under different step torque profiles and amplitudes. Time and frequency domain analyses of measured signals suggest that the accelerometers on the shaft and torsion arm (as partially reported in [1]) pick up some contributions from the shaft flexural modes and/or rigid body modes (of the experimental system) and therefore are not used for further analyses. Predictions from the minimal order, non-linear torsional models are in good agreement with new measurements. Only double sided impacts are observed in the single and dual clearance configurations under a step down torque from $\bar{T}$ = 1.0 to 0. The time periods of impacts, though sensitive to the precise values of clearance transitions, confirm a softening non-linearity. Discrepancies in measurements and models are mainly attributed to an absence of the Hertzian stiffness and impact damping type formulations; these should be pursued in future studies. Both predictions and measurements are quantified and assessed using six impulsive metrics as previously suggested by the literature on vehicle clunk problem [18,19] though the peak-peak amplitude of the impact (Q_3) is found to better describe the intensity of dominant impulsive events in the current experiment.

Studies from the eigensolutions and step responses of analogous linearized systems of the experiment suggest that the underlying linear system behavior may be used to better understand and qualitatively explain some behavior of systems with clearances. For instance, the peak amplitude ratio vector (**R**) from non-linear impulsive responses is useful as it matches well with the linear system eigenvectors. Finally, the validated non-linear models are used to examine the effect of alternate excitation profiles and amplitude on the step down or up responses (including for an exponentially decaying torque input). Predictions show that the excitation amplitude has a significant influence on the time varying periods. In fact, the 3DOF torsional system with three concurrent clearances (Case VIII) shows vastly different results as a transition from the double sided to single sided impacts is seen and the accompanying time periods suggest a hardening trend with a period doubling effect though minor chaos is also found (unlike other cases that have been examined). These observations will guide the formulation of future experimental and computational studies. The contributions of this article should enrich the non-linear dynamics literature especially on the transient responses and associated vibro-impact phenomena [6–9,32] while providing some benchmark studies for future investigators.

Acknowledgments

The authors would like to thank the member organizations of the Smart Vehicles Concepts Center (www.SmartVehicleCenter.org) as well as the National Science Foundation Industry/University Cooperative Research Centers program (www.nsf.gov/iip/iucrc) for supporting this work.

Appendix A. List of symbol

Symbols	
a_o, a_1, a_2	coefficients of curve fit for measured time periods
C	equivalent viscous damping coefficient
C	viscous damping matrix
h	Coulomb friction coefficient
J	torsional inertia
J	inertial matrix
k	torsional stiffness
K	stiffness matrix
N	modal torque vector
P	peak of low frequency sinusoid

Q	metric used to quantify impacts
R	peak amplitude ratio vector
S	short term Fourier transform
t	time
T	external (excitation) torque
T	torque (excitation) vector
T_d	dynamic torque
U	eigenvector matrix
$\mathscr{F}$	Fourier transform
Θ	stage transition (angular)
$\mathbf{\Lambda}$	eigenvalue matrix
Φ	elastic torque
Ψ	dissipation torque
Ξ	unit step (Heaviside) function
β	torque decay term
$\boldsymbol{\eta}$	modal (normal coordinate) vector
$\theta, \dot{\theta}, \ddot{\theta}$	angular displacement, velocity and acceleration
$\boldsymbol{\theta}(t)$	displacement vector
$\boldsymbol{\theta}(0_+)$	initial displacement vector
λ	diagonal elements of eigenvalue matrix
σ	regularizing factor
τ	time period
ω	circular frequency (rad/s)
ω_{rd}	damped natural frequency
ζ	damping ratio
Superscripts	
–	normalized
C	predicted value
M	measured value
pp	peak to peak
T	transpose of a matrix/vector
$\wedge$	re-normalized and approximated vector
Subscripts	
0	initial point at t = 0
I, II	stiffness stage indices
A, B, C	absolute coordinate or element indices
AB, BC	relative coordinate or element indices
e	combined inertia (A and B)
eff	effective inertia
f	final point
n	natural
osc	time varying
r	modal index
Abbreviations	
di	dual sided impact
DOF	degree of freedom
si	single sided impact
STFT	Short Term Fourier Transform

References

[1] M.D. Krak, R. Singh, Development of a scientific torsional system experiment containing controlled single or dual-clearance non-linearities: examination of step-responses, Mech. Syst. Signal Process. 84 (2017) 598–614, http://dx.doi.org/10.1016/j.ymssp.2016.07.026.
[2] F. Shaver, Manual Transmission Clutch Systems, SAE, 1997.
[3] J.P. Den Hartog, Mechanical Vibrations, fourth ed., McGraw-Hill, New York, 1956.
[4] S. Dubowsky, F. Freudenstein, Dynamic analysis of mechanical systems with clearances Part 2: dynamic response, ASME J. Eng. Ind. 93 (1971) 310–316, http://dx.doi.org/10.1115/1.3427896.
[5] Ph. Couderc, J. Callenaere, J. Der Hagopian, G. Ferraris, A. Kassai, Y. Borjesson, L. Verdillon, S. Gairmard, Vehicle driveline dynamic behavior: experimentation and simulation, J. Sound Vib. 218 (1998) 133–157, http://dx.doi.org/10.1006/jsvi.1998.1808.
[6] R.A. Ibrahim, Recent advances in nonlinear passive vibration isolators, J. Sound Vib. 314 (2008) 371–452, http://dx.doi.org/10.1016/j.jsv.2008.01.014.
[7] V.I. Babitsky, V.L. Krupenin, Vibration of Strongly Nonlinear Discontinuous Systems, Springer, Berlin, 2001.

[8] M.D. Krak, R. Singh, Practical and controlled laboratory vibration experiments that demonstrate the impulsive response of multi-staged clutch dampers, INTER-NOISE 2015, paper no. 58, San Francisco, USA, 9–12 August 2015.
[9] M.D. Krak, J.T. Dreyer, R. Singh, Step-response of a torsional device with multiple discontinuous non-linearities: formulation of a vibratory experiment, Mech. Syst. Signal Process. 70–71 (2016) 1117–1130, http://dx.doi.org/10.1016/j.ymssp.2015.08.013.
[10] T.E. Rook, R. Singh, Dynamic analysis of a reverse-idler gear pair with concurrent clearances, J. Sound Vib. 182 (1995) 303–322, http://dx.doi.org/10.1006/jsvi.1994.0198.
[11] Y.S. Choi, S.T. Noah, Forced periodic vibration of unsymmetric piecewise-linear systems, J. Sound Vib. 121 (1988) 117–126, http://dx.doi.org/10.1016/S0022-460X(88)80064-6.
[12] Y.B. Kim, S.T. Noah, Stability and bifurcation analysis of oscillators with piecewise-linear characteristics: a general approach, ASME J. Appl. Mech. 58 (1991) 545–553, http://dx.doi.org/10.1115/1.2897218.
[13] T.C. Kim, T.E. Rook, R. Singh, Effect of non-linear impact damping on the frequency response of a torsional system, J. Sound Vib. 281 (2005) 995–1021, http://dx.doi.org/10.1016/j.jsv.2004.02.038.
[14] J.Y. Yoon, R. Singh, Effect of multi-stage clutch damper characteristics on transmission gear rattle under two engine conditions, Proc. IMechE. Part D: J. Automobile Eng. 277 (2013) 1273–1295.
[15] R.J. Comparin, R. Singh, An analytical study of automotive neutral gear rattle, ASME J. Mech. Des. 112 (1990) 237–245, http://dx.doi.org/10.1115/1.2912598.
[16] L. Li, R. Singh, Analysis of vibration amplification in a multi-staged clutch damper during engine start-up, Proc. IMechE. Part D: J. Automobile Eng. 229 (2015) 1406–1418, http://dx.doi.org/10.1177/0954407014563362.
[17] A.R. Crowther, R. Singh, N. Zhang, C. Chapman, Impulsive response of an automatic transmission system with multiple clearances: formulation, simulation, and experiment, J. Sound Vib. 306 (2007) 444–466, http://dx.doi.org/10.1016/j.jsv.2007.05.053.
[18] A.R. Crowther, C. Janello, R. Singh, Quantification of clearance-induced impulsive sources in a torsional system, J. Sound Vib. 307 (2007) 428–451, http://dx.doi.org/10.1016/j.jsv.2007.05.055.
[19] W. Oh, R. Singh, Examination of clunk phenomena using a non-linear torsional model of a front wheel drive vehicle with manual transmission, SAE paper 2005-01-2291, 16–19 May 2005.
[20] J.S. Gurm, W.J. Chen, A. Keyvanmanesh, T. Abe, A.R. Crowther, R. Singh, Transient clunk response of a driveline system: laboratory experiment and analytical studies, SAE Int. J. Passeng. Cars - Mech. Syst. 6 (2008) 2007-01-2233. http://dx.doi.org/10.4271/2007-01-2233.
[21] J.W. Biermann, B. Hagerodt, Investigation of the clonk phenomenon in vehicle transmissions – measurement, modelling, and simulation, Proc. IMechE Part K: J. Multi-body Dyn. 213 (1999) 53–60, http://dx.doi.org/10.1243/1464419991544054.
[22] M.T. Menday, H. Rahnejat, M. Ebrahimi, Clonk: an onomatopoeic response in torsional impact of automotive drivelines, Proc. IMechE. Part D: J. Automobile Eng. 213 (1999) 349–357, http://dx.doi.org/10.1243/0954407991526919.
[23] M. Gnanakumarr, S. Theodossiades, H. Rahnejat, M. Menday, Impact-induced vibration in vehicular driveline systems: theoretical and experimental investigations, Proc. Inst. Mech. Eng. Part K J. Multi-Body Dyn. 219 (2005) 1–12. http://dx.doi.org/10.1243/1464419053577626.
[24] T. Abe, M. Felice, Driving the next generation powertrain NVH refinement thru virtual design. ISMA 2010, paper no. 665, Leuven, Belgium, 20–22 September 2010.
[25] C. Chae, Y. Lee, K. Won, K. Kang, Experimental and analytical approach for identification of driveline clunk Source & transfer path, SAE Trans. J. Passeng. Cars - Mech. Syst. 6 (2004) 2004-01-1231. http://dx.doi.org/10.4271/2004-01-1231.
[26] M. Krak, J. Dreyer, R. Singh, Development of a non-linear clutch damper experiment exhibiting transient dynamics, SAE Int. J. Passeng. Cars - Mech. Syst. 8 (2015) 754–761, http://dx.doi.org/10.4271/2015-01-2189.
[27] A. Saleh, M. D. Krak, J. T. Dreyer, and R. Singh, Development of refined clutch-damper subsystem dynamic models suitable for time domain studies, SAE Int. J. Passeng. Cars - Mech. Syst. 8 (2015) 2015-01-2180. http://dx.doi.org/10.4271/2015-01-2180.
[28] M. Wiercigroch, V.W.T. Sin, Experimental study of a symmetrical piecewise base-excited oscillator, ASME J. Appl. Mech. 65 (1998) 657–663, http://dx.doi.org/10.1115/1.2789108.
[29] J. Wojewoda, A. Stefański, M. Wiercigroch, T. Kapitaniak, Hysteretic effects of dry friction: modelling and experimental studies, Philos. Trans. R. Soc. 366 (2008) 747–765, http://dx.doi.org/10.1098/rsta.2007.2125.
[30] J. Ing, E. Pavlovskaia, M. Wiercigroch, Dynamics of a nearly symmetrical piecewise linear oscillator close to grazing incidence: modelling and experimental verification, Nonlinear Dyn. 46 (2006) 225–238, http://dx.doi.org/10.1007/s11071-006-9045-9.
[31] M.D. Todd, L.N. Virgin, Natural frequency considerations of an impact oscillator, J. Sound Vib. 194 (1996) 452–460, http://dx.doi.org/10.1006/jsvi.1996.0370.
[32] G. Kerschen, K. Worden, A.F. Vakakis, J.C. Golinval, Past, present and future of nonlinear system identification in structural dynamics, Mech. Syst. Signal Process. 20 (2006) 505–592, http://dx.doi.org/10.1016/j.ymssp.2005.04.008.
[33] T.C. Kim, T.E. Rook, R. Singh, Effect of smoothening function on the frequency response of an oscillator with clearance non-linearity, J. Sound Vib. 263 (2003) 665–678.
[34] Data Acquisition System, Model NI cDAQ-9184, National Instruments. <http://sine.ni.com> (accessed December 2016).
[35] Solidworks, Dassault Systemes. <http://www.solidworks.com> (accessed December 2016).
[36] Translational Accelerometer, Model 355B02, PCB Piezotronics Inc. <http://www.pcb.com> (accessed December 2016).
[37] MATLAB, MathWorks. http://www.mathworks.com/products/matlab/ (accessed December 2016).
[38] H. Jiang, M. Wiercigroch, Geometrical insight into non-smooth bifurcations of a soft impact oscillator, IMA JAM 81 (2016) 662–768, http://dx.doi.org/10.1093/imamat/hxw004.
[39] S. Banerjee, J. Ing, E. Pavlovskaia, M. Wiercigroch, R.K. Reddy, Invisible grazings and dangerous bifurcations in impacting systems: the problem of narrow-band chaos, PRE 79 (2009) 037201, http://dx.doi.org/10.1103/PhysRevE.79.037201.